NRMP-24-026 Vaz

X-ray magnetic circular dichroism

C. A. F. Vaz^{1†}, G. van der Laan^{2*}, S. A. Cavill³, H. A. Dürr⁴, A. Fraile Rodríguez^{5,6}, F. Kronast⁷, W. Kuch⁸,

Ph. Sainctavit⁹, G. Schütz¹⁰, H. Wende¹¹, E. Weschke¹², F. Wilhelm¹³

¹Swiss Light Source, Paul Scherrer Institut, Villigen PSI, Switzerland

²Diamond Light Source, Harwell Science and Innovation Campus, Didcot, United Kingdom

³School of Physics, Engineering and Technology, University of York, York, United Kingdom

⁴Department of Physics and Astronomy, Uppsala University, Uppsala, Sweden

⁵Department of Condensed Matter Physics, University of Barcelona, Barcelona, Spain

⁶Institute of Nanoscience and Nanotechnology (IN2UB), University of Barcelona, Barcelona, Spain

⁷Department Spin and Topology in Quantum Materials, Helmholtz-Zentrum Berlin für Materialien

und Energie, Berlin, Germany

⁸Institute of Experimental Physics, Freie Universität Berlin, Berlin, Germany

⁹Institute of Mineralogy, Physics of Materials and Cosmochemistry, CNRS, Sorbonne University

MNHN, Paris, France

¹⁰Max Planck Institute for Intelligent Systems, Stuttgart, Germany

¹¹Faculty of Physics, University of Duisburg-Essen, Duisburg, Germany

¹²Institute Quantum Phenomena in Novel Materials, Helmholtz-Zentrum Berlin für Materialien und

Energie, Berlin, Germany

¹³European Synchrotron Radiation Facility, Grenoble, France

[†]email: carlos.vaz@psi.ch

*email: Gerrit.vanderlaan@diamond.ac.uk

Abstract | X-ray magnetic circular dichroism (XMCD) is the difference in X-ray absorption between left and right circularly polarized light in magnetic materials. It is the X-ray counterpart of the magneto-optic effect for visible light, but shows a magnetic contrast up to three orders of magnitude higher. The exploration of XMCD using high-flux, monochromatic and polarization-variable synchrotron sources has advanced the understanding of magnetism and magnetic materials, in particular, when combined with spectral analysis based on powerful sum rules — this enables the quantification of spin and orbital moments with elemental, even chemical, selectivity and high sensitivity. As an essential cornerstone of techniques to probe magnetic nanostructures and spin

1

textures as well as their dynamics, XMCD has become an indispensable tool for the study of

magnetism at the nano- and atomic scale. This Primer provides an overview of the principles and physics underlying XMCD, the experimental techniques used to measure it, and its application to the study and understanding of fundamental and technologically relevant magnetic phenomena.

Web summary

X-ray magnetic circular dichroism (XMCD) is a powerful, element-specific technique that probes the spin and orbital magnetic moments of materials. By utilizing circularly polarized X-rays, XMCD enables detailed exploration of magnetic structures, including spin textures and dynamic behaviours. This Primer delves into the fundamental principles of XMCD, its application in advanced imaging methods, and analytical approaches for investigating a wide array of magnetic phenomena.

[H1] Introduction

X-ray magnetic circular dichroism (XMCD) is a magneto-optical effect [G] that describes the difference in X-ray absorption between left and right circularly polarized radiation by a magnetized material. It is an effect that is particularly strong at atomic X-ray absorption edges [G] and is used as an element-specific probe of magnetism in materials — for example, to determine the presence of a magnetic moment and quantify its spin and orbital components. It has been applied to the study of a wide range of systems, including ferromagnetic, ferrimagnetic and paramagnetic materials, in which for the latter the magnetic moment is induced by an external magnetic field or through proximity to a magnetized interface. XMCD shares the unique advantages of near-edge X-ray absorption spectroscopy (XAS): it is local (at the atomic scale), and offers elemental and chemical selectivity, sensitivity to specific orbitals, and moderate to large penetration depths (1 nm to 10 μm, depending on photon energy and detection method) with the flexibility to adjust the probing depth. Compared with magneto-optical effects in the visible region, the X-ray magnetic cross section [G] can be three orders of magnitude higher, amounting to a large fraction of the XAS absorption edge, especially at the L_{2,3} edges of transition metals (3d^N \rightarrow 2p⁵ 3d^{N+1}) and at the M_{4,5} edges of the rare earths (4f^N \rightarrow $3d^9 4f^{N+1}$) — the main constituents of technologically important magnetic materials. The local nature of the excitation permits an analytical treatment with sum rules used to relate the integrated intensities of the XMCD signals over the absorption peaks to the element-specific spin and orbital magnetic moments in the ground state — the latter a fundamental quantity that cannot be straightforwardly measured otherwise¹. Other methods, such as ferromagnetic resonance and polarized neutron diffraction, lack element specificity and sensitivity down to submonolayer atomic clusters^{2,3}.

The advent in the 1980s of dedicated synchrotron-radiation sources that provided energy-tuneable polarized X-rays marked the beginning of the exploration of magnetic dichroism in this spectral region^{4, 5, 6, 7}. XMCD has since become an indispensable tool for the characterization of magnetic systems, for example: for studying multicomponent, weak or diluted magnetic moments, as well as interfacial and two-dimensional (2D) materials; as a contrast mechanism for high-spatial-resolution magnetic imaging techniques used to investigate magnetic heterogeneity, domain structures, magnetic solitons, chiral magnets, in addition to interfacial cross-coupling between magnetic and electrical properties in multiferroic nanostructures; in determining the element specific fast time response of a spin system to external excitations; and in reciprocal-space techniques to determine underlying periodicities and spin chirality of topological materials.

The XAS process is governed by selection rules that conserve the total angular momentum in the transition between the initial state (atom and photon) and the excited state. An intuitive way of understanding XMCD is given by the two-step model for the $L_{2,3}$ edge of transition metals (Fig. 1). In the first step, a circularly polarized photon [G] excites a spin-polarized electron [G] from the spinorbit-split 2p core level (the Fano effect)⁸. Using the electric-dipole selection rules ($\Delta m_l = \pm 1$ and Δm_s = 0, for orbital angular momentum m_l and spin angular momentum m_s , in units of \hbar), it can be shown that, from the $2p_{3/2}$ level (L₃ edge), X-rays with positive helicity [G] (right circularly polarized) excite 62.5% spin-up electrons, and those with negative helicity (left circularly polarized) excite 37.5% spin-up electrons; from the $2p_{1/2}$ level (L_2 edge), a positive helicity excites 25% spin-up and negative helicity excites 75% spin-up electrons^{3, 9, 10}. In the second step, the dependence of the transition probability on the spin-up and spin-down density of empty states in the valence band comes into play: in a nonmagnetic material, where the unoccupied density of states for both spin-up and spin-down states are equal, the absorption of left and right circularly polarized light is the same; however, when an imbalance exists between the number of empty spin-up and spin-down states, the absorption is different for the two opposite photon polarizations and, when the spin moment is larger than the orbital moment, the absorption difference changes sign between the L_2 and L_3 edges. This is the XMCD effect and its energy dependence is the XMCD spectrum (Fig. 1). More generally, the absorption process is sensitive to both spin and orbital polarization of the final states above the Fermi level. In many cases, well-defined sum rules can be used to obtain the effective spin and orbital moments directly from the XMCD spectra. Nevertheless, extracting quantitative information for the magnetic characteristics can be challenging and may require expertise in physical models and computational methods.

The extension of X-ray microscopy techniques to measure XMCD permits the magnetic imaging of nanostructures with nanometre-scale spatial resolution and element specificity. Hence XMCD has been applied to image a plethora of magnetic solitons [G] (such as vortices, skyrmions, hopfions and nano oscillators)^{11, 12, 13, 14, 15} and other technologically relevant nanomagnetic structures of interest for spintronics. Another strength of XMCD — because it relies on a photon instead of an electron or magnetic-dipole probe (such as in magnetic force microscopy) — is that it does not disturb the magnetic state of the sample. Coherent imaging methods for XMCD, including vector ptychotomography and laminography, now provide near wavelength-limited resolution of a few nanometres to probe magnetic textures down to fundamental length scales in magnetism, which is critical for obtaining insights into the complex behaviour of magnetization distributions in all spatial dimensions.

In addition, the inherent time structure of synchrotron light — typically a pulse length of 10–100 ps — enables the study of fast magnetization dynamics in the GHz frequency range ¹⁶. More sophisticated sources, including femtosecond slicing in synchrotron radiation facilities and X-ray free electron lasers (XFELs) reach the fs range. Time-resolved X-ray microscopy provides a unique combination of 15-nm spatial resolution and 10-ps time resolution ¹⁷, giving access to the dynamical and switching behaviours of spin-based logic and magnonic devices.

Examples of the application of XMCD include the study of molecular magnetic systems^{18, 19, 20}, multilayers and magnetic van der Waals materials^{21, 22, 23}, magnetic domain-wall logic^{13, 24, 25}, magnetic monopoles in meta-lattices^{26, 27}, magnetic proximity effects at interfaces^{28, 29, 30}, and the dynamics of ultrafast demagnetization processes^{17, 31} — demonstrating the high potential of XMCD to address magnetic phenomena across a wide range of materials systems. Access to the orbital polarization provides a unique approach to the study of spin–orbit Dzyaloshinskii–Moriya interactions, quantum phenomena in strong spin–orbit-coupling materials with dominant Kitaev exchange interactions^{32, 33, 34}, and future pure orbital-related fundamental physical phenomena and their technological impact (for example, modern spin–orbit-torque-based devices^{35, 36}).

The capability of XMCD to probe a wide variety of systems and a very diverse set of quantum mechanical effects has made it a fundamental tool for the study of novel magnetic phenomena and new materials systems. In this Primer we provide an entry point to the XMCD effect and highlight its strengths and limitations, through a discussion of its microscopic underpinnings and exposition of

different methods and techniques. A flavour of XMCD's capabilities is given through a number of representative case studies that illustrate the potential of XMCD to investigate a vast range of magnetic phenomena.

[H1] Experimentation

[H2] Instrumentation

Any XMCD experiment needs a source of circularly polarized X-rays, and these are readily available at synchrotron-radiation facilities, most of which nowadays have XMCD beamlines³⁷. Synchrotron radiation is produced when electrons, travelling at relativistic energies in a confined orbit, are accelerated by magnetic devices such as dipole bending magnets, wigglers or undulators^{38, 39}. Circular polarization is induced in various ways: when passing through dipole magnets, the electrons generate radiation linearly polarized in the plane of the electron orbit, but with a circular component of opposite helicity above and below the orbit plane; in undulators, a spatially varying magnetic field pattern forces the electrons into helical orbits⁴⁰ (Fig. 2a).

At present, a fourth generation of diffraction-limited synchrotron light sources is coming online, with the benefits of ultrahigh brightness and high lateral coherence for imaging and scattering-based techniques. The ultimate X-ray source is an XFEL, in which coherent bunching of electrons, as they travel through a long undulator, is induced through feedback of the X-ray radiation produced by the electrons; the X-ray beam has full lateral coherence down to the diffraction limit and has a fs-scale time structure⁴¹. Laser-excited plasmas are becoming increasingly important in the production of X-rays — now reaching the keV X-ray regime⁴² and, with suitable polarizers, making XMCD experiments feasible. By design, these sources can provide ultrashort X-ray pulses and are suitable for dynamical studies⁴³.

X-rays are monochromatized by energy-dispersive elements, such as diffraction crystals⁴⁴, gratings^{40,45} or reflection zone plates⁴⁶. For soft X-rays [G] (the low-energy region of the spectrum, 0.1–2.0 keV), beamlines are windowless from the X-ray source to the sample and use an optical layout consisting of a glancing incidence mirror (to remove unwanted harmonic radiation and heat load), a grating monochromator, entrance and exit slits (defining flux and energy resolution), and a refocusing mirror to focus the beam onto the sample. For measurements of the magnetic saturated state, XMCD is then obtained as the difference of absorption scans taken with opposite light polarization or magnetic field directions. The most reliable data are usually obtained when alternating both the magnetic field and X-ray helicity [G] (that is, changing between right and left

circular polarization)⁴⁷. To minimize the impact of residual instabilities, X-ray absorption scans can be taken 'on the fly', with the monochromator and undulator gap changing synchronously while data are taken continuously — this reduces the acquisition time but has similar statistics and energy resolution to a step-by-step measurement. Some soft X-ray beamlines use line-gratings to reach 4 keV, covering the range of tender X-rays [G] (2–4 keV), but at the expense of a large intensity loss.

Standard hard X-ray [G] beamlines are based on a double-crystal monochromator, a mirror and a focusing section (to reject higher-order harmonics and to focus the beam to a few µm). Circular polarization can be produced either directly by helical undulators^{48,49} or by a diamond or silicon quarter wave plate^{50,51,52} (limited to energies greater than 2.8 keV owing to absorption losses). By combining fast switching of the polarization at every energy value with a phase-sensitive (lock-in) detection scheme⁵³, high quality XMCD data can be obtained. For completeness, we mention the existence of hard X-ray beamlines (5–20 keV) based on energy-dispersive optics^{54,55}: although restricted to transmission experiments, the absence of mechanical movement of the energy-dispersive spectrometer and the shorter acquisition time for a full spectrum makes energy-dispersive beamlines attractive for high-pressure XMCD studies using diamond anvil cells (up to 300 GPa) and for pulsed magnetic field measurements⁵⁶. Which energy range of X-rays to utilize is determined by the material to be studied and the absorption edges on which XMCD needs to be measured.

A key component in any XMCD experiment is a tuneable magnetic field capable of manipulating the sample's magnetic state. For analysing soft magnetic materials, magnetic fields up to a few mT can be produced by magnetization coils. Iron yokes can be added to increase the field up to 1 T; higher fields up to 17 T can be provided by superconducting solenoids for the study of paramagnets, hard magnetic systems, and quantum materials with complex and frustrated magnetic structures. Several experimental stations at synchrotron radiation facilities are equipped with three-dimensional vector magnets, usually with a large field of 7–9 T along the beam direction and 1–2 T in the perpendicular direction. For still larger magnetic fields, pulsed magnets can provide peak fields of up to 40 T for ~20 ms ^{57, 58}, suitable for studying hard-axis behaviour of hard magnetic materials, superconductors across the critical field, and quantum phase transitions ⁵⁹. Further possibilities for the sample environment include high pressure cells ^{60, 61, 62}, electric fields to manipulate magnetism in magnetoelectric materials ⁶³, visible light to induce magnetic switching in molecular complexes ⁶⁴, variable temperatures down to 200 mK ^{65, 66, 67}, and various characterization tools ⁶⁸. A recent development is the probing of the XMCD response simultaneously with the macroscopic

magnetization, volume changes or caloric properties of magnetic materials. This has proven beneficial in oxides, hydrides and nitrides to provide insights into magneto-structural phase transitions, in addition to fundamental Kondo physics and the exotic behaviours shown by rare-earth systems^{69, 70, 71, 72, 73, 74}. Similar studies have also been performed on technologically relevant magnetocaloric materials⁷⁵.

[H2] Experimental setup

X-ray absorption, and hence XMCD, can be measured either in transmission or by detecting the electron or fluorescence yield from the sample surface.

X-ray transmission is measured by the attenuation of the X-ray beam propagating through a sample of thickness t according to the Lambert–Beer law: $I_t(t) = I_0 \exp(-\mu t)$. Here, $I_t(t)$ is the transmitted beam intensity, I_0 is incident x-ray beam intensity, and $\mu = \mu(E)$ is the energy-dependent X-ray absorption coefficient. Direct transmission measurements require a sample thickness that is of the order of the attenuation length $(1/\mu)$ at the energy of interest, typically in the μ m range for hard X-rays²⁶ and down to ~20 nm for soft X-rays. In the latter case, ultrathin samples can be supported on freestanding SiN membranes⁷⁷. Some samples can be grown as crystalline films on thick transparent substrates that show X-ray excited optical luminescence, and this effect can be used as a measure of the X-ray intensity transmitted through the film⁷⁸. The advantage of transmission measurements is the straightforward determination of the total absorption cross section. The method is bulk sensitive: it probes the full sample volume exposed to the X-rays. It is also the method of choice for most time-resolved studies.

The X-ray absorption process creates photoelectrons, including primary photoemitted electrons, Auger electrons, and a cascade of secondary electrons that act as a gain multiplier, resulting in a photocurrent of a few pA to nA. Electrons with energies lower than 100 eV have an escape depth in solids (<10 nm) that is much smaller than the X-ray attenuation length, and the photocurrent is proportional to μ (ref. ⁷⁹). The most common way to detect this photocurrent is using a picoammeter to measure the drain current between sample and ground, known as total-electron yield (TEY) detection. Samples must be sufficiently conducting for TEY detection, but it provides very high surface sensitivity, owing to the short escape depth of the emitted electrons. This is advantageous for thin films, nanostructures and nanoparticles, but less so for studying bulk materials. Furthermore, the method requires clean surfaces and ultrahigh-vacuum conditions. TEY can also be recorded using an external electron detector, which, in combination with a bandpass or high-energy

filter, can be tuned to be particularly surface sensitive (by measuring partial electron yield, PEY)⁸⁰; this detection mode is, however, restricted to small magnetic fields. The differences between XAS measured in transmission and TEY in a multilayered sample are shown in Fig. 2b.

Following X-ray absorption, the resonantly excited core hole states in the sample can also decay through the emission of resonant and non-resonant fluorescence photons that can be readily detected by a photodiode to obtain the total fluorescence yield (TFY). This method is more bulk sensitive than TEY and can be applied to any material, independent of sample conductivity. However, the method suffers from some drawbacks: for soft X-rays, the TFY signal is typically much weaker than that for TEY ⁸¹ and requires a large detector placed near the sample. More critically, TFY is not exactly proportional to the absorption coefficient, because the resonant decay processes that contribute to TFY depend on the excited multiplet states, which are also polarization-dependent ^{82,83}. In addition, many of the fluorescence photons resonate with sample excitations and self-absorption can be substantial, leading to saturation effects and to distortions of the measured absorption spectra ⁸⁴. This effect is very strong for the M_{4,5} transitions of the rare earths, particularly in high-concentration bulk materials. Self-absorption effects are weaker in the case of dilute systems, thin films and nanostructures, and in the hard X-ray regime, where the X-ray cross-section is smaller.

A way to circumvent this problem and, generally, to increase the signal-to-noise ratio is to use an energy-selective detector to measure partial fluorescence yield (PFY) ⁸⁵; a related method is called inverse partial fluorescence yield (IPFY). Here, the energy bandpass of the fluorescence detection is tuned to a non-resonant X-ray emission (such as a resonance of a different core electron or of a different element in the material). The fluorescence from this core level is now reduced when sweeping across the resonant core-level excitation, providing a measure of the absorption as in a transmission experiment⁸⁶.

[H3] Spectromicroscopy. A number of microscopy techniques have been developed for acquiring XMCD data with high spatial resolution, whether at a specific spectroscopic feature (spectromicroscopy), or as a sequence of images taken as a function of photon energy or other parameters (microspectroscopy)^{87,88}. XMCD magnetic imaging techniques can be used to study spatial variations of magnetic phenomena especially in micro- and nanosized elements⁸⁹; to correlate magnetic domain configurations with composition in inhomogeneous samples⁹⁰; to investigate magnetic phase transitions^{91,92} and order-parameter coupling between different ferroic systems⁹³; to identify local changes in spin and orbital moments^{91,94}; and to study dynamic

processes, on time scales from geological⁹⁵ to the propagation of spin waves^{96, 97, 98} or ultrafast magnetization dynamics triggered by optical stimuli⁹⁹. The most common techniques for magnetic Xray imaging available at synchrotron facilities are X-ray photoemission electron microscopy (XPEEM), transmission X-ray microscopy (TXM), scanning transmission X-ray microscopy (STXM), and X-ray ptychography, which is an advanced form of coherent diffraction imaging, or CDI (Fig. 3, Table 1). The angle of incidence of the X-ray beam determines the direction of magnetic contrast. By recording image series for different rotation or tilt angles, 2D and three-dimensional (3D) vector maps of the magnetization or, in the case of transmission experiments, even tomograms can be obtained^{14,100}. Additionally, we mention X-ray Fourier-transform holography (Table 1), in which an interference pattern of the scattered beam is recorded on a charge-coupled-device camera and then computationally reconstructed. This bulk-sensitive technique has been used successfully for imaging of magnetic vortex dynamics^{17, 101} and 3D tomographic imaging of the magnetization vector field¹⁰². Scattering techniques involve both the real part of the index of refraction and the imaginary part (absorption), and require a higher-order treatment of the light interaction cross-section; techniques such as holography and ptychography can extract both components — the so-called phase problem (Fig. 3e).

Techniques based on photoelectron detection, such as XPEEM, require essentially a surface that is conductive and smooth. The short inelastic mean free path of electrons makes these techniques more sensitive to surfaces and interfaces, with probing depths of 1–10 nm. Because the imaging relies on electron optics, application of magnetic fields during imaging is very limited. Nowadays, the spatial resolution of XPEEM is in the range of 25–50 nm; PEEM instruments equipped with aberration correctors have a potential resolution in the 2 nm range¹⁰³, but this resolution has not been achieved yet with X-rays. One powerful advantage of XPEEM is that it is capable of complementary measurements, including X-ray photoelectron spectroscopy and Fermi surface mapping¹⁰⁴. An example of results obtained using XMCD–XPEEM is shown in Fig. 3b.

Techniques based on photon detection in transmission, such as STXM, holography or CDI, require X-ray-translucent samples. STXM uses a very fast integrating detector and is well suited to dynamic measurements¹⁰⁵. X-ray ptychography, the most common form of CDI, acquires diffraction images by illuminating multiple overlapping regions on the sample. Owing to redundant information in the diffraction images, image reconstruction from ptychographic data is particularly robust. While in STXM the spatial resolution, defined by the microfocus of the X-ray beam, is in the range of 10–30

nm 106 , in ptychography the theoretical resolution is diffraction-limited: recent results show a resolution of 5 nm 107 .

[H3] X-ray detected ferromagnetic resonance. Traditional ferromagnetic resonance (FMR) has been widely used to determine key magnetic parameters in thin films by analysing resonance frequencies (linked to internal and applied fields) and relaxation (assessed through the damping of the resonance). The novel technique of X-ray detected FMR (XFMR) enables the examination of element-specific magnetization dynamics through XMCD¹⁰⁸. XFMR measures both the amplitude and phase of the spin precession in chemically distinct layers. One experimental challenge is that the spin precession frequency is in the GHz range, and the precession cone angle is less than 1°. The solution involves stroboscopic measurements that leverage the synchrotron's time structure (approximately 500 MHz). By synchronizing the radio-frequency field driving the spin precession with the X-ray pulses using the synchrotron's clock, each X-ray pulse captures the magnetization cone at the same phase of the precession cycle. In short, XFMR integrates FMR and XMCD as pump and probe techniques, respectively. More recently, XFMR has also been conducted using diffraction and reflection geometries, providing additional research opportunities¹⁰⁹.

[H2] Sample requirements

TEY measurements are sensitive to the topmost surface layers, which can have differences in stoichiometry, chemical potential, valence state, hybridization and magnetic anisotropy compared to the bulk. Therefore, in situ surface preparation, including cleavage of bulk samples or sputter cleaning, is an important capability in many experimental setups. Otherwise, air-sensitive samples need to be capped by a suitable material (such as C, Au, Pt, Al, Ru or Ta); these capping layers must be ultrathin (<3 nm), continuous and conductive. Importantly, they should not modify the magnetic properties of the underlying material through proximity effects, hybridization or displacement reactions (for example, magnetic oxides might be reduced by an Al capping layer¹¹⁰ and formation enthalpies must be carefully considered). High-atomic-number materials with large spin—obit coupling (such as Pt) can also modify the magnetic properties¹¹¹.

Poor surface conductivity leads to charging effects, which modify the intensity of the TEY signal collected. The extent of charging is often evident in one of three ways: periodic noise in the spectra due to regular charge—discharge processes; a time-dependent response in the TEY to a sudden change in the incident photon intensity (such as shutter opening); and reduced intensity ratios between L_3 and L_2 , due to the larger absorption and charging effect at L_3 compared with the L_2 edge.

Charging can be partially compensated by biasing the sample with a large negative voltage (\sim -50 V). However, measurement of magnetic insulators (such as yttrium iron garnet) can still be performed using TEY if the insulator is capped with a conductive material^{112, 113} or the measurement is performed in an inert-gas atmosphere such as helium¹¹⁴.

For measurements of transmission and TFY, the concerns noted above for TEY are relaxed because the sample does not need to be conductive and the surface region is small compared to the total sample thickness. Transmission and TFY are also better suited for the study of buried layers and buried interfaces. For high-resolution spectroscopy, the sample should be uniform (in thickness and composition) over an area exceeding the X-ray footprint. This is important for angle-dependent measurements, where the footprint varies as $1/\sin\theta$, where θ is the angle between the incident beam and surface plane.

In the soft X-ray region, XMCD is usually measured under high or ultrahigh vacuum conditions and the samples must be vacuum-compatible; for low-temperature measurements, the presence of residual gas molecules such as water, CO or CO₂ can lead to condensation on the sample surface that reduces the TEY signal. Radiation damage is also a concern. Although inorganic materials are mostly radiation-resistant, the intense X-ray beams available at third- and fourth-generation sources combined with the lack of heat dissipation and vacuum environment can lead to sample damage, such as reduction of transition-metal oxides¹¹⁵. For organic samples, the situation is worse. The X-ray beam often modifies the sample directly or indirectly, owing to photoelectron irradiation that can break chemical bonds¹¹⁶. In such cases, the photon flux can be reduced or the beam can be repositioned to different areas of the sample before the damage becomes measurable.

[H1] Results

[H2] Background theory and model fitting

Because, in the XAS or XMCD process, the core hole involves a local excitation, an atomic approach is an appropriate starting point. A suitable atomic Hamiltonian is

$$H_{\text{atom}} = H_{\text{el}} + H_{\text{LS}} + H_{\text{LF}} + H_{\text{Zeeman}},\tag{1}$$

where H_{el} gives the electrostatic (Coulomb and exchange) interactions, H_{LS} the spin—orbit interaction, H_{LF} the ligand- or crystal-field interaction, and H_{Zeeman} the interaction with an applied magnetic field. In localized many-electron systems, transitions are of the type $p^6 d^N \rightarrow p^5 d^{N+1}$ for $L_{2,3}$ edges of d-metals, or $d^{10}f^N \rightarrow d^9f^{N+1}$ for $M_{4,5}$ edges of f-metals. The wavefunctions ψ_i and ψ_f of the initial- and final-state configurations with energies E_i and E_f are calculated in intermediate coupling using an

atomic Hartree–Fock code with relativistic correction¹¹⁷, where the spin–orbit and electrostatic interactions appear on an equal footing. In such multiplet codes, the Hartree–Fock values of the Slater parameters are generally reduced to 70–80% to account for configuration interaction and screening effects. The spin–orbit parameters, however, usually agree with their atomic values within a few percent. Crystal- and ligand-field interactions can be incorporated into the multiplet code using symmetry considerations, which are most effective in high-symmetry ionic systems¹¹⁸. For example, in a cubic environment there is only one empirical parameter — the octahedral or tetrahedral crystal-field parameter 10Dq — while all other parameters are determined by atomic theory. Additionally, charge-transfer interactions can be included similarly to the Anderson impurity model, using the intra-atomic Coulomb interaction (Hubbard U) for a $2p^63d^N$ ground state, where $U = E(2p^63d^{N-1}) + E(2p^63d^{N+1}) - 2E(2p^63d^N)$; the core–valence Coulomb interaction is included by a parameter Q and the ligand-to-metal charge transfer by $\Delta = E(2p^63d^{N+1}\underline{L}) - E(2p^63d^N)$, where \underline{L} represents a hole on the ligands.

The transition probability T_{if} from ψ_i to ψ_f is given by Fermi's golden rule as

$$T_{if} \propto \left| \left\langle \psi_f | \mathbf{A} \cdot \mathbf{p} | \psi_i \right\rangle \right|^2 \delta(E_f - E_i - \hbar \omega),$$
 (2)

where the first factor gives the modulus square over the matrix element $\langle . | . | . \rangle$ and the second factor is the delta distribution for energy conservation in the excitation process. The operator ${\bf A}={\bf \epsilon}e^{i{\bf k}\cdot{\bf r}}$ is the vector potential of the incident photon and ${\bf p}$ the momentum of the electron; ${\bf \epsilon}$ and ${\bf k}$ are the unit polarization vector and wave vector, respectively, of the incident photon with energy $\hbar\omega$, ${\bf r}$ is the position vector. For ${\bf k}\cdot{\bf r}\ll 1$, the exponential factor can be expanded as $e^{i{\bf k}\cdot{\bf r}}=1+i{\bf k}\cdot{\bf r}+\cdots$, which yields the E1 electric-dipole [G] and E2 electric-quadrupole [G] terms, respectively. The E1 approximation holds well in the soft X-ray region, giving a transition operator ${\bf \epsilon}\cdot{\bf r}$, so that absorption of left and right circularly polarized photons results in $\Delta m_l=-1$ and +1 transitions. Hence, circular dichroism occurs when the magnetic sublevels in the ground state are unequally populated, due to the presence of magnetism or a magnetic field. For the E2 term, which becomes observable in the hard X-ray region, transitions up to $\Delta m_l=\pm 2$ are allowed. A detailed theoretical foundation can be found in refs $^{3,\,118,\,119}$.

Various computer codes based on multiplet theory are available to calculate XMCD — for example, Cowan^{117, 120}, CTM4XAS¹²¹ and Quanty¹²², among others. These codes differ mainly in their graphical interface but all give essentially the same calculated spectra; they, as well as band-structure codes, are described in more detail in refs ^{3,123}. Once the multiplet structure has been calculated, it can be compared with the experimental XMCD spectra (either by visual inspection or using a least-squares

fit procedure) to extract quantitative information about the magnetic properties of the material, such as spin and orbital moments or magnetic ordering (Fig. 4a).

This theoretical approach has been very successful — the first calculations correctly predicted the expected spectra $^{124,\,125}$ — but important quantitative information can also be obtained directly from experimental data by using the powerful spin and orbital sum rules, which are essentially theory-independent. The sum rules give the relation between integrated intensities and the ground-state expectation values of the spin and orbital moments, $\langle S_z \rangle$ and $\langle L_z \rangle$; for the case of the L_{2,3} edge of transition metals, they have the form $^{126,\,127}$:

$$\langle L_z \rangle = 2 \frac{\int (\mu_- - \mu_+) dE}{\int (\mu_- + \mu_+ + \mu_0) dE} \langle n_h \rangle \tag{3}$$

$$\langle S_z \rangle + \frac{7}{2} \langle T_z \rangle = \frac{3}{2} \frac{\int_{L_3} (\mu_- - \mu_+) dE - 2 \int_{L_2} (\mu_- - \mu_+) dE}{\int (\mu_- + \mu_+ + \mu_0) dE} \langle n_h \rangle, \tag{4}$$

where $T=\sum_i \mathbf{s}_i-3\mathbf{r}_i(\mathbf{s}_i,\mathbf{r}_i)/r_i^2$ is the magnetic dipole term whose diagonal elements describe the difference in charge asymmetry between the spin up and down electrons³; $n_{\rm h}$ is the number of holes in the d band; and μ_- , μ_+ and μ_0 are the x-ray absorption coefficients for circular left, circular right, and linear polarised light with electric field parallel to the magnetisation, respectively. The first sum rule states that the integral of the XMCD signal is proportional to the orbital moment averaged over the thermally occupied levels of the ground state and a related sum rule applies for the K edge¹²⁶. The second sum rule states that a fixed linear combination of the XMCD spin—orbit split signals yields the spin moment $\langle S_z \rangle$ plus a contribution from the magnetic dipole term $\langle T_z \rangle$, often together denoted as the effective spin moment.

Alternatively, single-particle calculations can be conducted using density functional theory either in real space through methods such as multiple scattering and wavefunction approaches, or in reciprocal space using band-structure methods. Electrons can be analysed in both spaces, but the real-space basis is particularly well suited for core-level absorption calculations. Additionally, these techniques are applicable to molecules or liquids, which do not have periodic structures. Notable real-space single-electron codes for calculating XAS include FEFF and FDMNES as well as various quantum-chemistry codes 123.

[H2] Measurement goals

Two kinds of XMCD results can be distinguished. The first type concerns the K and L edges of transition elements, for which, using sum rules^{126, 127}, the spin and orbital moments of the magnetic ground state can be extracted. A second type (which includes the deeper absorption edges of 4f

lanthanides and 5f actinides, and anions and ligands) refers to cases for which a quantitative analysis is not possible because of the simultaneous presence of E1 and E2 transitions. For such experiments, the approach is to determine a magnetic signature and record its variation as a function of an external parameter such as temperature, external magnetic field, or pressure.

[H3] L_{2,3} edge of transition metals. XMCD has been measured for all 3d elements from scandium to copper^{130, 131, 132, 133, 134, 135, 136, 137}; for 4d elements including Y, Mo, Ru, Rh, Pd and Ag ^{138, 139, 140, 141, 142, 143}; and for 5d elements including W, Re, Ir, Pt and Au ^{144, 145, 146, 147, 148, 149}. In the E1 approximation, the L_{2,3} edges probe the valence d states.

[H3] K and L_1 edges. XMCD at the K edges has also been measured, mainly for 3d metals. In the E1 approximation, they give access to the empty p levels and to the antibonding part of the chemical bond or the conduction electrons in a metallic bond. For K and L_1 edges, the orbital angular momentum of the core hole is zero, spin—orbit coupling does not split the core level and no information can be gained about the spin moment. In addition to the main component of the K edges ($1s \rightarrow p$ transitions), transitions associated with E1 transitions toward p—d hybridized states and E2 transitions towards d states are generally observed in the pre-edge region. The application of sum rules for E2 transitions to extract quantitative magnetic moments is difficult, usually requiring ligand-field multiplet calculations 150 . When inversion symmetry breaking allows p—d hybridizations — for example, in the tetrahedral point group (S_4 , D_{2d} and T_d , among others) — E1 transitions are enhanced in XMCD and a finite E1 signal is superimposed on the E2 signal. These XMCD signals can be used for magnetometry under the assumption that the XMCD signal follows the total magnetic moment of the absorbing ions.

[H3] 4f lanthanides and 5f actinides. The second category of elements to which XMCD is applied includes the 4f lanthanides¹⁵¹ and 5f actinides¹¹⁹. In the E1 approximation, the 4f or 5f orbitals are probed at the M_{4,5} edges, creating a 3d core hole. The 4f and 5f levels can also be probed through E2 transitions by recording the L_{2,3} edges. For lanthanides (or actinides), information is then collected on the 5d (6d) levels via E1 transitions, on which is superimposed information on the 4f (5f) levels via E2 transitions. Although a quantitative analysis is generally not possible in this case, the different temperature and angular dependences of the E1 and E2 XMCD cross sections for the 5d and 4f levels, and for the 6d and 5f levels, can aid in separating E1 from E2 transitions^{152, 153, 154}.

[H3] Anions and ligands. The second category for XMCD also includes anions or ligands. In simple solid-state models, anions are not considered to carry a magnetic moment. For instance, in magnetite, Fe₃O₄, the electronic structure is usually interpreted as $[Fe^{3+}]_A [Fe^{2+}Fe^{3+}]_B O_4^{2-}$ with magnetic moments originating from the ferrimagnetic coupling of the Fe³⁺ ions on the A sites (T_d symmetry) and Fe²⁺ and Fe³⁺ ions on the B sites (D_{3d} symmetry)¹⁵⁵. Indeed, the outer orbital of O^{2-} is O^{2+} and no magnetic polarization is expected. However, because of O^{2+} and hybridization, the O^{2+} and is partially unoccupied giving a finite O^{2+} magnetic moment, resulting in XMCD at the O^{2+} edge^{156, 157}. XMCD has also been detected on ions such as Ge, P, S, Cl, I, Ga and Te, which contain no apparent open shell with either d or f symmetry^{60, 158, 159, 160, 161, 162, 163}.

[H2] Data analysis

The first two XMCD sum rules, Eqs (3) and (4), were developed in the E1 approximation^{126, 127}. The sum rules are most accurate when the orbital absorbing the excited core electron is localized. In the presence of extended orbitals, the closure relation needed for sum-rule derivation is no longer strictly valid and sum rules cannot be rigorously applied^{164, 165}. The cases where both E1 and E2 transitions are present are more challenging; sum rules for E2 transitions exist, but their application is cumbersome because they involve the calculation of higher-order momenta^{166, 167, 168}. Hence, it follows that the sum rules are most appropriate for the L_{2,3} edges of transition metals and M_{4,5} edges of lanthanides or actinides (but see also the section 'Limitations and optimizations').

Data treatment often aims to prepare raw XMCD data for application of the sum rules. The first consideration is the nature of the detection mode. Has the XMCD been recorded in transmission, TEY or TFY? (PFY measured at resonance is not a good measure of the X-ray absorption because the assumption that the fluorescence probability of the level of interest is independent of incident photon energy breaks down for resonant X-ray emission; non-resonant IPFY does not suffer from this limitation⁸⁶.) Depending on the type of measurement, corrective measures must be taken.

In transmission, the cross section is given by $\ln(I_0/I)$ and the sample should be homogeneous (of constant thickness without pinholes) to avoid deformation of the XAS spectra (for which there are no reliable corrective measures^{135, 169}). Today, most examples of XMCD recorded in transmission have been measured on beamlines working in the dispersive mode in the hard X-ray range. In this case, there is generally no I_0 signal, although the signal recorded in the absence of the sample can be employed in its place.

Except at very low grazing angles⁸⁴, in TEY there is no reabsorption because the penetration depth of the X-rays is usually much larger than the escape depth of the electrons (<10 nm)^{170, 171, 172}. The derivation of the sum rules is in fact made for μ /($4\pi^2\alpha\hbar\omega$), where α is the fine structure constant, so the experimental x-ray absorption coefficient μ should be divided by the photon energy $\hbar\omega$ before applying the sum rules. However, few researchers consider this correction necessary, mainly because the TEY is not exactly proportional to μ^{173} .

In TFY, there are well known reabsorption effects, which need to be corrected. Although reabsorption effects are small when the absorbing atom is diluted, they must always be corrected for a quantitative application of the sum rules¹⁷⁴. In the case of hard X-rays, the fluorescence (reabsorption) corrections are straightforward to compute^{174, 175}. In the soft X-ray range, the energy⁸² and angular dependence¹⁶⁵ of the fluorescence decay introduce changes to the XAS spectra that prevent a quantitative use of the sum rules.

To apply the sum rules, the isotropic spectrum (μ_{lso}) must be determined. The integrated isotropic cross-section is proportional to the number of holes¹⁷⁶. In the case of a magnetically polarized crystal, the isotropic x-ray absorption in the E1 approximation is obtained by averaging the spectra for left (μ_-), right (μ_+), and linear (μ_0 , with electric field parallel to **M**) polarized light, cf. denominators of Eqs. (3) and (4). Often (μ_- + μ_+)/2 measured with **k** along **M** is taken as a first approximation for the isotropic x-ray absorption. When X-ray natural or magnetic linear dichroism is absent, (μ_- + μ_+)/2 = μ_{lso} , but this is generally not correct and such an approximation can introduce severe flaws in the application of the sum rules^{137, 177}.

A final correction of the XAS spectra involves removing the background contribution corresponding to transitions to the continuum. For $L_{2,3}$ edges, this is often handled by removing two arctangent curves in a 2:1 ratio for which the inflection points are at the maxima of the L_3 and L_2 edges with width equal to the convolution of the instrumental and lifetime broadening (Fig. 4b,c). It should be noted that this procedure is only approximate and usually not suitable for ionic compounds¹⁷⁸. The true position of the continuum onsets, however, can be obtained from a comparison of XAS with core-level photoemission¹⁷⁹.

For E1 transitions, reversing either the magnetization or the circular polarization is equivalent; however, in the general case where E2 transitions are also present, the equivalence does not hold because cross-terms between matrix elements involving E1 and E2 might be nonzero (see

Supplementary Information). When the sample is a powder and when the orientation point group of the space group of the crystal is not compatible with the observation of optical activity, the equivalence between reversing the magnetic field and reversing the helicity is preserved. In the cases where optical activity is present^{167, 180}, reversing the X-ray helicity is different from reversing the external magnetic field because the E1–E2 cross terms are not zero. These E1–E2 terms are at the origin of X-ray natural circular dichroism and X-ray magneto-chiral dichroism^{118, 180, 181}.

[H2] Statistical analysis and error calculations

As discussed above, quantitative determination of the spin and orbital moments relies on several theoretical assumptions and experimental approximations that introduce systematic errors in the general application of the sum rules. Those errors are difficult to quantify but comparative measurements have shown that the sum rules can provide total moments within ~10% of the value measured using bulk techniques^{168, 182, 183} (see also the section 'Limitations and optimizations'). In addition, because the XMCD sum rules require the integration of a difference signal, good statistics is important; often a good strategy is to acquire several spectra at a moderate accumulation time, or to switch helicity at each energy point to minimize signal drift.

[H1] Applications

The XMCD effect has been applied to study a multitude of magnetic systems and magnetic phenomena: detailed accounts can be found in refs ^{3, 7, 10, 44, 184, 185, 186, 187, 188, 189, 190}. Although we have emphasized the quantitative aspects of XMCD above, the effect is also widely used as a sensitive and element-specific intrinsic probe of magnetic order. In the following, we illustrate the use of XMCD in a few topical areas in magnetism.

[H2] Magnetism of thin films and nanostructures

The first applications of XMCD concerned the study of 2D magnetism in ultrathin films, including the link between magnetic anisotropy and orbital moment^{191, 192}. For example, XMCD measurements at the spin-reorientation transition of ferromagnetic materials as a function of thickness¹⁹³, or induced by an adjacent magnetic layer of a different element⁹¹, demonstrated the theoretically predicted relationship^{192, 194} between the orbital moment anisotropy and the magnetocrystalline anisotropy energy. Applied to single Co adatoms and nanoparticles, XMCD revealed the magnetic anisotropy at the atomic scale². The element selectivity and high sensitivity of XMCD is often exploited to detect induced magnetic moments in nominally nonmagnetic materials that are in contact with a

magnetized ferromagnetic material, either at an interface or as an alloy (for example, in Cu in Co/Cu and Fe/Cu multilayers $^{28, 195, 196}$, Co $_{90}$ Cu $_{10}$ alloys 28 or in artificial FeCu alloys 197), or to detect a net magnetization induced at the interface of an antiferromagnetic material by the presence of an adjacent ferromagnetic layer 198,199 . XMCD is also sensitive to the magnetization induced by a strong external magnetic field 200 , an effect used, for example, in the study of magnetic molecules.

XMCD in TEY is ideal for the measurement of structures at reduced dimensionality and size, including single atoms adsorbed on surfaces. Sum-rule analysis of XMCD spectra has shown that, when going from bulk material over a monoatomic layer to single-atomic chains²⁰¹ or to individual adatoms²⁰², quenching of the orbital moment is successively reduced and the spin moment approaches the single-atom limit. Studies of the blocking of the direction of the magnetic moment of dispersed non-interacting paramagnetic adatoms on surfaces — important for the long-term goal of reaching room-temperature stability of the magnetic moment — can thus be carried out using XMCD and have culminated in the observation of magnetic remanence of individual Ho atoms adsorbed on ultrathin MgO layer on Ag(100) at 30 K (ref. ²⁰³).

XMCD has also been extensively used to study magnetic nanostructures and nanoparticles, often in combination with X-ray microscopy. For example, XPEEM has been employed to image the magnetic configuration of thin films and patterned structures, leading to a better understanding of the contribution of the different terms to the magnetic energy, the role of interlayer interaction in 2D van der Waals materials (Fig. 3b), or of the lateral geometry and local defects in small magnetic structures²⁰⁴. In addition, it has been used to image and probe individual magnetic nanoparticles with sizes smaller that the microscope resolution (using an approach similar to super-resolution microscopy)^{205, 206}, establishing the presence of enhanced magnetic anisotropy in Fe and Co nanoparticles due to the presence of local defects, as determined by correlative XPEEM and STEM measurements^{207,208}. Moreover, STXM and X-ray holography imaging have been employed to study the static and dynamic behaviour of magnetic skyrmions (Fig. 3d) and other topological spin structures (Fig. 3c)^{11, 17, 209, 210, 211, 212, 213}. More recently, a new class of magnetic systems has been unveiled which are nominally antiferromagnetic but with the spins sitting on non-equivalent crystal lattice sites with broken inversion symmetry, named altermagnets²¹⁴. The break in inversion symmetry leads to unusual magnetic phenomena, including the presence of a marked XMCD effect ²¹⁵, which has been employed to probe the local spin order in MnTe²¹⁶.

[H2] Quantum materials and molecular magnets

Quantum materials are systems whose properties are ruled by quantum effects that cannot be described classically, such as quantum entanglement and quantum phase transitions. Examples include Kitaev materials, which are characterized by spin frustration and a strong spin—orbit coupling that leads to spin and orbital entangled states forming so-called pseudo-1/2 spin states, and which are susceptible to hosting a spin-liquid phase^{32, 33, 217}. By providing access to both orbital and spin moments, XMCD has the potential to provide insights into the physics of these materials, and has already been explored, for example, to determine the sign of the trigonal crystal field of the Co 3d states in the Kitaev-candidate material Na₃Co₂SbO₆ (ref. ³⁴).

XMCD is also useful for the study of novel material properties at the intersection between magnetism and topology, such as in topological insulators, which are characterized by metallic surface states protected by time-reversal symmetry²¹⁸. In particular, it has been predicted that inducing a magnetic moment in the metallic surface state could lead to the onset of Majorana quasi particle states²¹⁹, and XMCD has been exploited to determine the onset of magnetism in topological insulators by doping^{220, 221} or by contact to a ferromagnetic layer^{222, 223}. For example, Arrott–Noakes plots — obtained by measuring the XMCD of Dy at the M₅ edge as a function of field at low temperatures — have been used to obtain the transition temperature of Dy-doped Bi₂Te₃ topological insulator thin films²²¹.

The control of the quantum spin state in 2D systems, including hybrid (paramagnetic) molecules, 2D van der Waals magnets and other low-dimensional materials^{18, 19, 20, 23, 224}, is also of outstanding interest. For magnetic molecular complexes, a fundamental understanding of the interaction at the interface (also termed 'spinterface', refs ^{225,226}) requires monolayer or submonolayer molecular coverages. Planar molecules such as porphyrin or phthalocyanine have been widely studied in this context, because they adsorb flat in the submonolayer regime on ferromagnetic substrates. In these cases (for example, Fe-porphyrin molecules adsorbed on Ni(100), ref. ¹⁸), the element specificity of the XMCD technique enables the study of 3d metal atom magnetism in the molecule separately from the ferromagnetic metal film, including element-specific hysteresis curves and determination of the nature and strength of the magnetic coupling. The tailoring of the magnetic coupling of the paramagnetic atoms in the molecules to the substrates, which is essential for applications, can be achieved by utilizing intermediate light atoms such as oxygen or carbon (graphene)^{227, 228}.

A different class of fascinating magnetic molecules are the so-called double-decker molecules consisting of a lanthanide atom between two phthalocyanine molecules. Because of the large single-

ion anisotropy of the lanthanides, these molecules can exhibit magnetic hysteresis without coupling to a ferromagnetic substrate 229 . However, coupling to ferromagnetic substrates can indeed be mediated by graphene 230,231 . Utilization of graphene advances new concepts, because specific 2D systems can only be synthesized on graphene 232 . For example, the weak van der Waals interaction of europium cyclooctatetraene (EuCot) molecules with graphene enables the synthesis of EuCot nanowires which wind up and build a 2D nanocarpet (Fig. 5a, inset). Interestingly, XMCD studies have revealed a hysteretic behaviour for these nanowire systems which appears at 5 K and vanishes at 7 K, demonstrating that this system exhibits ferromagnetic behaviour (Fig. 5a). In addition, quantitative XMCD measurements showed that Eu displays a saturation spin moment of 7.0±0.6 μ_{B} /atom at 5 K expected for Eu²⁺ and a zero orbital moment (within the error bars), Fig. 5b. The latter result is unexpected, given the large magnetic anisotropy reflected in the magnetic hysteresis

Spin-crossover molecules (SCOs) show promise for applications in molecular spintronics, sensors and displays. The spin state of these molecules can be switched from a low-spin to a high-spin state by, for example, visible light irradiation, or changes in temperature or pressure²³³. SCO complexes have been identified for which, with the help of XAS studies, light-induced excited spin-state trapping at near room temperature is seen²³⁴.

[H2] Magnetization dynamics and ultrafast processes

The demand for faster, denser data storage and processing capabilities continues to propel efforts to find novel ways of controlling magnetic states. One example is the potential for spin currents flowing across interfaces to switch and manipulate magnetization, for example, via spin—orbit torques²³⁵. Such effects usually occur on sub-ns timescales and are ideally probed using the fast time resolution of synchrotron radiation together with high-resolution XMCD imaging techniques^{96, 236}. The development of sub-100-fs laser pulses has enabled radically new ways of manipulating magnetism ²³⁷. In such studies, excitation of the electronic system with a spin-conserving optical laser pulse is used to study the subsequent magnetization dynamics, including the influence of magnetic exchange interactions, spin—orbit coupling and electron- and spin-lattice coupling^{235, 237}. Examples include the application of the sum rules to determine the spin and orbital dynamics in 3d metals^{238, 239} and their role in angular-momentum transfer to the lattice²⁴⁰; and the element-specific magnetization dynamics in CoFeGd alloy films, showing that all-optical magnetization switching proceeds via transient ferromagnetic coupling of the magnetic subsystems²⁴¹.

Many of these ultrafast studies have been carried out using so-called fs-slicing of ps-long bunches at synchrotron sources such as BESSY II ²⁴², and are important stepping stones towards the use of XFEL radiation for XMCD. However, the most important recent development for XMCD studies at XFELs²⁴³ is the ongoing installation of helical insertion devices ²⁴⁴, to generate circular polarization, at most major European XFEL facilities. The high X-ray flux of XFELs offers the exciting prospect of combining XMCD with holographic imaging²⁴⁵ and resonant magnetic scattering²⁴⁶. The potential of timeresolved XMCD studies is highlighted in ref. 247, and in Fig. 5. The ultrafast dynamical response of a metallic Co-Pd multilayer system to fast optical excitation promotes electrons from below the Fermi level (E_F) to above (Fig. 5c). This excitation process can be probed directly in XAS via additional core valence transitions below $E_{\rm F}$, and the bleaching of transitions into now occupied states above $E_{\rm F}$. The crossover between the two effects defines the position of $E_{\rm F}$ (Fig. 5d). It is then possible to perform sum-rule analysis in the time domain for individual energy states: a first attempt is shown in Fig. 5e, where the XMCD asymmetry can be viewed as a measure of the spin moment evolution; the observed changes have been assigned to the excitation of magnons²⁴⁷. Future measurements will be able to corroborate this result and assess whether, for example, all optical spin transfer is possible during laser excitation²⁴⁸.

[H1] Reproducibility and data deposition

A defining characteristic of X-ray spectroscopy is its sensitivity to small modifications in the electronic structure of materials. However, this also creates the difficulty that small variations in the system properties — such as internal strain, defects, non-stoichiometry and impurity phases affecting the magnetic moment — will also strongly impact the XAS and XMCD spectral features. Hence, although XMCD provides a fingerprint of the material, its reproducibility will depend largely on how well a given system can be reproduced to the smallest detail. Experimental conditions, such as energy resolution of the instrument, will also impact the XMCD line shape. As a consequence, no databases have yet been established for the deposition of XMCD standards, although they could be very beneficial to the community.

For data comparison, it is important that XAS spectra for both left and right circular polarization are provided; these are normally plotted with the pre-edge region set to zero and the post-edge set to one, giving an immediate reading of XMCD as a percentage. Note that for low concentrations, variations in background drift between the two spectra can complicate the obtaining of reliable difference signals. Additional important information includes the temperature, the magnetic-field

direction and history (for example, field cooled or zero-field cooled), the degree of circular and linear polarization, and the angle of incidence of the light. Estimates of the energy resolution can be more difficult to obtain but should be reported if possible. For data modelling, in particular for multiplet calculations, it is important not only that the code used is specified, but also what parameter values were used for the calculation; this can be easily achieved by making the input-parameter files available (as supplementary information or placed in a repository).

Beam damage, introducing (often) irreversible modifications in the atomic, electronic, and magnetic structure of the material, has a negative impact on the reproducibility of the XMCD spectrum and should be assessed, especially for less radiation-resistant materials. Control measurements carried out to determine the exposure damage threshold (which entails measuring the beam intensity) would largely address such a problem.

[H1] Limitations and optimizations

[H2] Sum rules

Experimentally, it is found that in most cases the sum rules apply, but there are some limitations^{10,} $^{168, 177, 249, 250, 251, 252, 253, 254, 255, 256}$, mostly associated with the determination of the number of holes for the magnetic open shell, the presence of hybridization or band structure in the ground state, E2 transitions¹⁵², energy dependence of the radial matrix elements^{257, 258}, the presence of the magnetic dipole term $\langle T_z \rangle$, and jj mixing of the spin-orbit split core states (where j refers to the quantum number of the total angular momentum of the core hole, for example j = 1/2 and 3/2 for a 2p core hole).

The precise number of 3d holes, n_h , is experimentally inaccessible since the absorption is not measured on an absolute scale. Instead, n_h is often estimated by chemical intuition, or by ligand-field multiplet or band-structure calculations, which may not always be representative for the actual material. Performing XMCD measurements on a set of reference samples with different oxidation states can help to narrow down the value of n_h^{259} . The spin sum rule has been theoretically simulated and tested in several works, and been compared to polarized neutron reflectivity results 182 . Because the ratio $\langle L_z \rangle / \langle S_z \rangle$ does not depend on n_h , relative changes in the orbital to spin moment can be obtained with higher certainty, for example, across a sample series.

The role of the $\langle T_z \rangle$ term is discussed in several works^{183, 192, 260, 261}. In octahedral symmetry, $\langle T_z \rangle$ is nearly zero at room temperature and large at temperatures for which 3d spin-orbit coupling causes

an unequal distribution over the states; for lower symmetry materials, $\langle T_z \rangle$ is essentially unaffected by the 3d spin—orbit coupling. Calculations based on density functional theory give large $\langle T_z \rangle$ values at the surface of 3d metals and neglecting them can give errors in $\langle S_z \rangle$ up to 50% for the Ni(001) surface 260 . One way to obtain $\langle T_z \rangle$ is to carry out XMCD measurements at different angles 190 . We note that the conclusion that $\langle T_z \rangle = 0$ in cubic systems $^{135, 262, 263}$ is based on the approximation that $\langle T_z \rangle = \langle \mathbf{Q}_z \rangle \langle S_z \rangle$ and that the charge quadrupole moment $\langle \mathbf{Q}_z \rangle = 0$ for cubic systems; however, in general, $\langle T_z \rangle = \langle \mathbf{Q}_z \cdot S_z \rangle \neq \langle \mathbf{Q}_z \rangle \langle S_z \rangle$ is found to be negligible $^{135, 263}$.

Another effect leading to an error in the spin sum-rule analysis is the jj mixing between the spin—orbit split core levels, L_2 and L_3 (or M_4 and M_5). If the energy splitting between the L_3 and L_2 edges is relatively small compared with other terms — such as Coulomb and exchange interactions, or crystal-field parameters — the final state wavefunction at the L_3 edge is not built from a pure $2p_{3/2}$ state but also contains some $2p_{1/2}$ contribution (likewise for the L_2 edge). This problem can be addressed in the spin sum rule by introducing a correction factor C, which can be estimated by comparing multiplet calculations with and without core hole electrostatic interactions^{3, 177}. While $C \approx 1$ for Fe d⁶ to Cu d⁹, C = 1.47 for Mn d^{5 266} and $C = 2 \pm 0.2$ for Cr d^{3 259}. For the rare earth $M_{4,5}$ edges, the value of C increases from 1.60 to 3.55 for Ce f¹ to Sm f⁵, but remains close to 1 for Gd f⁷ to Yb f¹³

The spin and orbital moments in most rare-earth elements are collinear (either parallel or antiparallel) owing to the strong 4f spin—orbit coupling, which results in levels with distinct values of the total angular momentum J (with Ce being a notable exception). This behaviour follows from a general principle concerning the effect of a small perturbation on a J level. According to the Wigner–Eckart theorem, the proportionality rule (equation (32) in ref. ²⁶⁷) indicates that operators of the same rank are proportional to the same tensor. For rank-1 tensors (that is, vectors), this means that $\langle L_2 \rangle$, $\langle S_2 \rangle$ and $\langle T_2 \rangle$ are proportional to the total angular momentum $\langle J_2 \rangle$. Consequently, these vectors are (anti)parallel and maintain a constant ratio, regardless of small perturbations such as crystal-field interactions. This consistency eliminates the need to apply sum rules, as the ratio of orbital to spin moments remains fixed, and the rule can even be used to verify the accuracy of the sum rules.

There are other limitations that are mainly due to the sample properties. When the absorbing ion is present in different valences at various sites, a quantitative application of the sum rule is not possible. In weak ferromagnets, such as α -Fe₂O₃, the antiferromagnetic coupling above the Morin

temperature between Fe ions prevents the determination of atomic spin and orbital moments; in addition, because the Fe ions are all equivalent in the magnetic space group, the sum rules yield values for $\langle L_z \rangle$ and $\langle S_z \rangle$ that are averaged over the unit cell.

[H2] Experimental limits

TEY exhibits saturation effects at shallow incidence angles⁸⁴, requires conducting samples, and the signal is heavily altered by magnetic fields even in spectral regions where XMCD is zero^{268, 269}. TFY suffers from self-absorption, compromising the accuracy of the XMCD sum-rule analysis^{270, 271}. X-ray excited optical luminescence (XEOL) has been introduced as a good, complementary detection method to overcome the shortcomings of TEY and TFY — however, weaknesses include its reliance on the (temperature-dependent) X-ray luminescence efficiency of the substrate ⁷⁸, on the target energy range not overlapping with substrate resonances, and on the requirement that the speed of data acquisition is slower than the luminescence decay from the substrate^{272, 273}. The magnetic moments obtained from XEOL-based XMCD sum rules give reliable results^{78, 274} within the commonly accepted 10% margin¹⁸³.

Another concern in XMCD experiments is the degree of circular polarization for each of the two helicities of the monochromatic beam, which depends both on the polarization of the radiation source and the transfer of polarization by the optical components^{44, 177}. This effect, which is more pronounced in the hard X-ray range, can be minimized by collecting pairs of spectra with opposite directions of the magnetization⁴⁴.

Element-specific hysteresis loops provide a unique way to access interlayer coupling in multilayers and spin valves, for example, to study exchange spring magnets²⁷⁵ and magnetic anisotropy. They are measured along easy and hard axes at fixed photon energy by ramping the field. However, TEY-based XMCD hysteresis loops can be problematic because of the effect of the applied field on the emitted electrons, especially around zero where the field direction switches sign. This can be avoided using TFY detection instead. Since XMCD hysteresis measurements are slow, the possibility for drifts in beam position and photon energy needs to be considered. For temperature-dependent measurements, thermal expansion or contraction of the cold finger may result in different regions of the sample being probed; ice accumulation at low temperatures can be prevented by cycling the sample to room temperature before such effects set in.

[H1] Outlook

[H2] Challenges in the field

In solid-state research, magnetism is an important field, where interest in basic and applied science and technologies is growing owing to innovations in ultrasensitive techniques and the synthesis of new materials systems with unexpected magnetic properties. XMCD-based approaches constitute indispensable tools to address a range of phenomena and material systems. Examples include magnetic solitons such as vortices, skyrmions and hopfions, and the unique properties of these topological textures are being explored for information storage and processing^{276, 277}. Newly discovered 2D van der Waals magnets and nanoscale 3D structures are enabling the design of artificial magnetic materials, but are highly sensitive to defects and magnetic frustration, and also exhibit complex band structures featuring new quasi-particle quantum states.

Among the main challenges for XMCD studies, the need for higher spatial resolutions — to approach the exchange length of materials (a few nm), down to the atomic level — can be met with higher polarized flux and advanced detectors for coherent imaging; a technique that links synchrotron X-rays and quantum tunnelling processes²⁷⁸ has made access to a single atom through X-ray absorption possible. Enhancing the sensitivity of XMCD to the C, N and O K-edges, and extending the study of so-called d⁰ magnetism to other elements and atomic excitations, is an ongoing challenge, as is understanding the behaviour of systems under direct stimuli, either to explore out-of-equilibrium processes or to optimize device performance. Further expanding the dynamical capabilities of XMCD to element-specific ferromagnetic and even paramagnetic resonance creates new possibilities in various systems. Correlative integration of XMCD directly with other techniques such as X-ray scattering, scanning tunnelling microscopy and magnetic resonance will lead to better understanding of the coupling between magnetism and other fundamental electronic properties.

From a theoretical perspective, accurately interpreting the XMCD spectra and extracting quantitative information about magnetic properties requires sophisticated theoretical models and data-analysis techniques. Robust analysis methods that account for complex interactions and experimental conditions will greatly enhance the amount of information that can be extracted from XMCD measurements, as well as improving the predictive power of XMCD spectroscopy and guiding experimental design.

Many of the challenges mentioned above are stimulating novel approaches to measure XMCD in materials, particularly at the nanoscale and on ultrafast time scales. Developments in diffraction-limited X-ray sources, XFELs and high-harmonic-generation sources are offering access to XMCD with

higher spatial resolution, higher repetition rates and shorter timescales. These sources are suitable for a range of X-ray microscopy methods: such as ptychography, which has now been extended from the hard to the soft X-ray range; and X-ray holography, which is being applied at XFELs for ultrafast magnetic microscopy, opening the door to probing magnetic nanostructures under extreme short and intense excitations, such as generated by terahertz laser pulses.

[H2] Future directions

[H3] Origin of magnetism in complex materials. Improving the sensitivity and spatial resolution of XMCD-based characterization techniques brings the potential to address the origin of magnetism in new materials systems, including disentangling contributions from different atomic sites, from interfaces or magnetic domains. Here, the exclusive access given by XMCD to orbital momenta and polarization is crucial in answering fundamental and technological questions, especially in strong spin—orbit coupling phenomena.

[H3] Response of magnetism to external stimuli. The development of time-resolved XMCD techniques to cover a wide range of timescales $(10^{-9}-10^{-16} \text{ s})$ will enable the study of the dynamics of magnetic phenomena in real time under external stimuli — relevant for understanding fast dynamical processes for ultrafast spin-based devices.

[H3] Magnetic interactions at nanoscale interfaces. Nanoprobe XMCD spectroscopy is enabling the investigation of magnetic interactions at nanoscale interfaces, disentangling multiple magnetic order parameters, and shaping the role of interface engineering in tailoring magnetic functionalities.

[H3] Insights into spintronic devices. Specifically, a better understanding of new 2D and van der Waals magnets and devices based on spin and orbital torques provided by the unique capabilities of XMCD to probe orbital and spin moments; in combination with other spectroscopic and imaging techniques, XMCD can provide insights into spin transport, spin polarization, and spin-dependent electronic structure, contributing to the development of next-generation spintronic technologies.

[H3] Design of magnetic materials. Advanced theoretical models and computational tools combined with experimental XMCD measurements will enable us to predict and design new magnetic materials with tailored properties.

[H3] Materials under extreme conditions. By extending XMCD experiments to high-pressure, external stress, in-situ/operando capabilities, high-temperature, sub-kelvin temperatures, ac fields, or ultrafast conditions, we can explore new magnetic states of matter and novel quantum phenomena.

[H2] Medium-term priorities

In summary, a number of priorities for the medium term will give a large payoff in terms of scientific outcome: (i) enhanced spatial resolution for XMCD microscopy techniques, (ii) developing pump-probe XMCD setups with femtosecond to picosecond temporal resolution, (iii) integrating XMCD spectroscopy with other imaging and microscopy techniques, (iv) improving the sensitivity of XMCD to elements with induced magnetism, (v) advancing XMCD experiments under realistic *operando* modes, (vi) strengthening the synergy between theoretical modelling and experimental measurements, and (vii) promoting broader accessibility to XMCD facilities and fostering collaboration between research groups and institutions worldwide, essential for advancing the field. These are ambitious goals, however, successfully addressing them will lead to further breakthroughs in XMCD spectroscopy, enabling researchers to gain deeper insights into the magnetic properties of materials and their applications in various technologies, including spintronics and magnonics, magnetic data storage, magnetic sensor technologies, bio-nanomedicine, and novel quantum systems.

[H1] References

- 1. Fernandez V. et al. Observation of orbital moment in NiO. Phys. Rev. B 57, 7870 (1998).
- 2. Gambardella, P. et al. Giant Magnetic Anisotropy of Single Cobalt Atoms and Nanoparticles. *Science* **300**, 1130 (2003).
- 3. van der Laan, G. & Figueroa, A. I. X-ray magnetic circular dichroism a versatile tool to study magnetism. *Coord. Chem. Rev.* **277–278**, 95–129 (2014). **An advanced-level text on theoretical and experimental aspects of XMCD.**
- 4. van der Laan, G. et al. Experimental proof of magnetic X-ray dichroism. *Phys. Rev. B* **34**, 6529–6531 (1986). **To our knowledge, this is the first experimental report of X-ray magnetic dichroism.**
- 5. Schütz, G. et al. Absorption of Circularly Polarized X Rays in Iron. *Phys. Rev. Lett.* **58**, 737 (1987). **This paper reports the observation of XMCD at the Fe K edge.**
- 6. Rogalev, A., Wilhelm, F., Jaouen, N., Goulon, J. & Kappler, J.-P. X-ray Magnetic Circular Dichroism: Historical Perspective and Recent Highlights. In *Magnetism: A Synchrotron Radiation Approach*, Beaurepaire, E., Bulou, H., Scheurer, F. & Kappler J.-P. (Eds.). Springer-Verlag Berlin Heidelberg 2006. 7. van der Laan, G. 25 years of magnetic X-ray dichroism, in Magnetism and Synchrotron Radiation: Towards the Fourth Generation Light Sources, Eds. Beaurepaire, E. Bulou, H. Scheurer, F. & Joly, L. *Springer Proceedings in Physics* **151**, 257-288 (2013). https://doi.org/10.1007/978-3-319-03032-6_9 8. Fano, U. Spin orientation of photoelectrons ejected by circularly polarized light. *Phys. Rev.* **178**, 131 (1969).
- 9. van der Laan, G. & Thole, B.T. Magnetic dichroism in the X-ray absorption branching ratio. *Phys. Rev. B* 42, 6670 (1990).
- 10. J. Stohr & H. Siegmann, Magnetism: from fundamentals to nanoscale dynamics (Springer, 2006). A reference book on magnetism and the interaction of polarized photons with matter, including ultrafast dynamics.
- 11. Moreau-Luchaire, C. et al. Additive interfacial chiral interaction in multilayers for stabilization of small individual skyrmions at room temperature. *Nature Nanotechnology* **11**, 444 (2016). **This article** reports the application of XMCD with microscopy to image skyrmion structures in asymmetric metallic multilayers with a net Dzyaloshinskii–Moriya interaction.
- 12. Wintz S. et al. Magnetic vortex cores as tunable spin-wave emitters. Nature Nanotechnology **11**, 948 (2026).
- 13. Beardsley R. P. et al. Deterministic control of magnetic vortex wall chirality by electric field. *Scientific Reports* **7**, 7613 (2017).
- 14. Donnelly C. et al. Three-dimensional magnetization structures revealed with X-ray vector nanotomography. *Nature* **547**, 328 (2017).

- 15. Kent, N. et al. Creation and observation of Hopfions in magnetic multilayer systems. *Nat Commun* **12**, 1562 (2021).
- 16. Pizzini, S. Vogel, J. Bonfim, M. & Fontaine, A. Time-Resolved X-ray Magnetic Circular Dichroism A Selective Probe of Magnetization Dynamics on Nanosecond Timescales, in Spin Dynamics in Confined Magnetic Structures II, Hillebrands & B. Ounadjela K. (Eds.), *Topics Appl. Phys.* **87**, 155-185 (2003).
- 17. Büttner, F. et al. Dynamics and inertia of skyrmionic spin structures. *Nature Physics* **11**, 225 (2015).
- 18. Wende, H., Bernien, M., Luo, J. et al. Substrate-induced magnetic ordering and switching of iron porphyrin molecules. *Nature Mater* **6**, 516–520 (2007).
- 19. Frisk, A., Duffy, L.B., Zhang, S., van der Laan, G., & Hesjedal, T. Magnetic X-ray spectroscopy of two-dimensional Crl₃ layers, *Materials Letters* **231**, 5-7 (2018).
- 20. Herper, H.C., Brena, B., Puglia, C., Bhandary et al. Molecular Nanomagnets: Fundamental Understanding. Springer Nature Singapore (2020).
- 21. Bedoya-Pinto A. et al. Intrinsic 2D-XY ferromagnetism in a van der Waals monolayer. Science **374**, 616 (2021).
- 22. Suzuki M. et al. Magnetic anisotropy of the van der Waals ferromagnet Cr₂Ge₂Te₆ studied by angular-dependent X-ray magnetic circular dichroism. *Physical Review Research* **4**, 013139 (2022).
- 23. Fujita, R. et al. Layer-dependent magnetic domains in atomically thin Fe $_5$ GeTe $_2$. ACS Nano **16**, 10545-10553 (2022).
- 24. Mawass M.-A. et al. Switching by Domain-Wall Automotion in Asymmetric Ferromagnetic Rings. *Phys. Rev. Applied* **7**, 044009 (2017)
- 25. Luo Z. et al. Current-driven magnetic domain-wall logic. *Nature* **579**, 214 (2020).
- 26. Mengotti E. et al. Real-space observation of emergent magnetic monopoles and associated Dirac strings in artificial kagome spin ice. *Nature Physics* **7**, 68 (2010).
- 27. Rana A. et al. Three-dimensional topological magnetic monopoles and their interactions in a ferromagnetic meta-lattice. *Nature Nanotechnology* **18**, 227 (2023).
- 28. Samant, M. G. et al. Induced spin polarization in Cu spacer layers in Co/Cu multilayers. *Phys. Rev. Lett.* **72**, 1112 (1994).
- 29. Figueroa, A. I. et al. Structural and magnetic properties of granular Co-Pt multilayers with perpendicular magnetic anisotropy. *Phys. Rev B* **90**, 174421 (2014).
- 30. Liu Y. et al. Induced Ti magnetization at $La_{0.7}Sr_{0.3}MnO_3$ and $BaTiO_3$ interfaces. *APL Mater.* **4**, 046105 (2016).

- 31. Yamamoto K. et al. Ultrafast demagnetization of Pt magnetic moment in L10-FePt probed by magnetic circular dichroism at a hard X-ray free electron laser. *New J. Phys.* **21**, 123010 (2019).
- 32. Jackeli, G. and Khaliullin, G. Mott Insulators in the Strong Spin-Orbit Coupling Limit: From Heisenberg to a Quantum Compass and Kitaev Models. *PRL* **102**, 017205 (2009).
- 33. Witczak-Krempa, W., Chen, G., Kim, Y. B, and Balents, L. Correlated Quantum Phenomena in the Strong Spin-Orbit Regime. *Annu. Rev. Condens. Matter Phys.* **5**, 57 (2014).
- 34. van Veenendaal, M et al. Electronic structure of Co 3d states in the Kitaev material candidate honeycomb cobaltate Na₃Co₂SbO₆ probed with X-ray dichroism. *Phys. Rev. B* **107**, 214443 (2023).
- 35. Manchon A. Current-induced spin-orbit torques in ferromagnetic and antiferromagnetic systems. *Rev. Mod. Phys.* **91**, 035004 (2019).
- 36. Xue F. et al. Field-free spin-orbit torque switching assisted by in-plane unconventional spin torque in ultrathin Pt/CoN. *Nature Communications* **14**, 3932 (2023)
- 37. Wilhelm, F. Magnetic Materials Probed with Polarized X-ray Spectroscopies. *Synchrotron Radiation News* **26**, 2-5 (2013).
- 38. Willmott, P. An Introduction to Synchrotron Radiation: Techniques and Applications. John Wiley & Sons Ltd. (2019).
- 39. Hwu, Y. & Margaritondo, G. Synchrotron radiation and X-ray free-electron lasers (X-FELs) explained to all users, active and potential. *J. Synchrotron Rad.* **28**, 1014 (2021).
- 40. Englisch, U. et al. The elliptical undulator UE46 and its monochromator beam-line for structural research on nanomagnets at BESSY-II. *Nuclear Instruments and Methods in Physics Research Section A: Accelerators, Spectrometers, Detectors and Associated Equipment* **467**, 541 (2001).
- 41. Pellegrini, C., Marinelli, A. & Reiche, S. The physics of X-ray free-electron lasers. *Rev. Mod. Phys.* **88**, 015006 (2016).
- 42. Popmintchev, T. et al. Bright Coherent Ultrahigh Harmonics in the keV X-ray Regime from Mid-Infrared Femtosecond Lasers. *Science* **336**, 1287 (2012).
- 43. Borchert, M. et al. *X-ray* magnetic circular dichroism spectroscopy at the Fe L edges with a picosecond laser-driven plasma source. *Optica* **10**, 450-455 (2020).
- 44. Rogalev, A. & Wilhelm, F. Magnetic circular dichroism in the hard X-ray range. *Phys. Met. Metallography* **116**, 1285 (2015).
- 45. Petersen, H., Jung, C., Hellwig, C., Peatman, W.B., & Gudat, W. Review of plane grating focusing for soft x-ray monochromators. *Rev. Sci. Instr.* **66**, 1 (1995).
- 46. Brzhezinskaya, M. A novel monochromator for experiments with ultrashort X-ray pulses. *J. Synchrotron Rad.* **20**, 522 (2013).

- 47. Holldack, K. et al. Flipping the helicity of X-rays from an undulator at unprecedented speed. *Commun. Phys.* **3**, 61 (2020).
- 48. Elleaume, P. Helios: a new type of linear/helical undulator, J. Synchrotron Rad. 1, 19–26 (1994).
- 49. Sasaki, S. et al. Design of a new type of planar undulator for generating variably polarized radiation, *Nucl. Inst. Meth. A* **331**, 763–767 (1993).
- 50. Belyakov, V. & Dmitrienko, V. Polarization phenomena in X-ray optics. *Sov. Phys. Usp.* **32**, 697–719 (1989).
- 51. Hirano, K., Izumi, K., Ishikawa, T., Annaka, S., Kikuta, S. An X-ray Phase Plate Using Bragg-Case Diffraction. *Jpn. J. Appl. Phys.* **30**, L407 (1991).
- 52. Bouchenoire, L., Morris, R. J. H. & Hase, T. P. A. A silicon <111> phase retarder for producing circularly polarized X-rays in the 2.1-3 keV energy range. *Appl. Phys. Lett.* **101**, 064107 (2012).
- 53. Suzuki, M. et al. Helicity-modulation technique using diffractive phase retarder for measurements of X-ray magnetic circular dichroism, *Jpn. J. Appl. Phys.* **37**, L1488–L1490 (1998).
- 54. Mathon, O. et al. XMCD under pressure at the Fe K edge on the energy-dispersive beamline of the ESRF. *J. Synchrotron Rad.* **11**, 423-427(2004).
- 55. Baudelet, F., Kong, Q., Nataf, L. & Cafun J.-D. ODE: a new beam line for high-pressure XAS and XMCD studies at SOLEIL, *High Press. Res.* **31**, 136–139 (2011).
- 56. Pascarelli, S. et al., The Time-resolved and Extreme-conditions XAS (TEXAS) facility at the European Synchrotron Radiation Facility: The energy-dispersive X-ray absorption spectroscopy beamline ID24, *J. Synchrotron Rad.* **23**, 353 (2016).
- 57. Yasumura, H. et al. 40 T Soft X-ray Spectroscopies on Magnetic-Field-Induced Valence Transition in Eu(Rh_{1-x}Ir_x)₂Si₂ (x = 0.3). Journal of the Physical Society of Japan **86**, 054706 (2017).
- 58. Yamamoto, S. et al. Field-induced magnetic transitions in the highly anisotropic ferrimagnet ErFe₅Al₇ studied by high-field X-ray magnetic dichroism. *Phys. Rev. B* **109**, 094404 (2024).
- 59. Matsuda, Y. H. et al. XMCD spectroscopy on valence fluctuating and heavy fermion compounds in very high magnetic fields up to 40 T. *J. Phys.: Conf. Ser.* **190**, 012019 (2009).
- 60. Wilhelm, F. et al. High pressure XANES and XMCD in the tender X-ray energy range. *High Pressure Research* **36**, 445 (2016).
- 61. Wilhelm, F. et al. Investigating the electronic states of UTe₂ using X-ray spectroscopy. Communication Physics **6**, 96 (2023).
- 62. Itie, J.-P., Baudelet F. & Rueff, J.-P. High Pressure XAS, XMCD and IXS, Ch. 14 in X-ray *Absorption and X-ray Emission Spectroscopy: Theory and Applications*, First Edition. Edited by Jeroen A. van Bokhoven and Carlo Lamberti. John Wiley & Sons, Ltd (2016).

- 63. Liu, H. et al. Soft X-ray spectroscopic endstation at beamline 08U1A of Shanghai Synchrotron Radiation Facility. *Rev. Sci. Instrum.* **90**, 043103 (2019).
- 64. Jafri, S. F. et al. Atomic Scale Evidence of the Switching Mechanism in a Photomagnetic CoFe Dinuclear Prussian Blue Analogue. *J. Am. Chem. Soc.* **141**, 3470-3479 (2019).
- 65. J-P. Kappler, et al. Ultralow-temperature device dedicated to soft X-ray magnetic circular dichroism experiments. *J. Synchrotron Rad.* **25**, 1727–1735 (2018).
- 66. Serrano, G. et al. Quantum dynamics of a single molecule magnet on superconducting Pb(111). *Nature Materials* **19**, 546-551 (2020).
- 67. Serrano, G. et al. Magnetic molecules as local sensors of topological hysteresis of superconductors. *Nature Communications* **13**, 3838 (2022).
- 68. Aubert, A. et al. Simultaneous Multi-Property Probing During Magneto-Structural Phase Transitions: An Element-Specific and Macroscopic Hysteresis Characterization at ID12 of the ESRF. *IEEE Transactions on Instrumentation and Measurement* **71**, 6002409 (2022).
- 69. Haskel, D. et al. Stability of the ferromagnetic ground state of La₂MnNiO₆ against large compressive stress. *Phys. Rev. B* **84**, 100403(R) (2011).
- 70. Ishimatsu, N. et al. Hydrogen-induced modification of the electronic structure and magnetic states in Fe, Co, and Ni monohydrides. *Phys. Rev. B* **86**, 104430 (2012).
- 71. Kawamura, N., Ishimatsu, N., Isshiki, M., Komatsu Y., & Maruyama, H. Ga magnetic polarization in Mn₃GaC under high pressure probed by Ga K-edge XMCD. *Physica Scripta* **T115**, 591–593 (2005).
- 72. Ding, Y. et al. Novel Pressure-Induced Magnetic Transition in Magnetite (Fe₃O₄). *Phys. Rev. Lett.* **100**, 045508 (2008).
- 73. Baudelet, F. et al. Absence of abrupt pressure-induced magnetic transitions in magnetite. *Phys. Rev. B* **82**, 140412(R) (2010).
- 74. Subías, G. et al. Investigation of pressure-induced magnetic transitions in $Co_xFe_{3-x}O_4$ spinels. *Phys. Rev. B* **87**, 094408 (2013).
- 75. Law, J. Y., Moreno-Ramirez, L. M., Díaz-García, Á., & Franco, V. Current perspective in magnetocaloric materials research. *J. Appl. Phys.* **133**, 040903 (2023).
- 76. Henke, B. L., Gullikson, E.M., & Davis, J. C. X-ray interactions: photoabsorption, scattering, transmission, and reflection at E=50-30000 eV, Z=1-92. *Atomic Data and Nuclear Data Tables* **54**, 181-342 (1993). https://henke.lbl.gov/optical_constants/
- 77. Shaw, J. M. et al. Quantifying Spin-Mixed States in Ferromagnets. *Phys. Rev. Lett.* **127**, 207201 (2021).

- 78. Piamonteze, C., Windsor, Y. W., Avula, S. R. V., Kirk, E. & Staub, U. Soft X-ray absorption of thin films detected using substrate luminescence: a performance analysis. *J. Synchrotron Rad.* **27**, 1289–1296 (2020).
- 79. Gudat, W. & Kunz C. Close similarity between photoelectric yield and photoabsorption spectra in the soft-X-ray range. *Phys. Rev. Lett.* **29**, 169 (1972).
- 80. Blobner, F., Neppl, S. & Feulner P. A versatile partial electron yield detector with large acceptance angle and well-defined threshold energy and gain. *J. Electron Spectrosc. Relat. Phenom.* **184**, 483 (2011).
- 81. Stöhr, J. X-ray magnetic circular dichroism spectroscopy of transition metal thin films. *J. Electron Spectrosc. Relat. Phenom.* **75**, 253 (1995).
- 82. de Groot, F. M. F., Arrio, M.A., Sainctavit, Ph., Cartier, C. & Chen, C.T. Fluorescence yield detection: why it does not measure the X-ray absorption cross-section. *Solid State Communications* **92**, 991-995 (1994).
- 83. de Groot, F. Dips and peaks in fluorescence yield X-ray absorption are due to state-dependent decay. *Nature Chem.* **4**, 766 (2012).
- 84. Nakajima, R., Stohr, J., & Idzerda, Y. U. Electron-yield saturation effects in L-edge X-ray magnetic circular dichroism spectra of Fe, Co, and Ni. *Phys. Rev. B* **59**, 642 (1999). **This paper highlights the impact of measurement and sample geometry on XMCD.**
- 85. Boyko T. D., Green, R. J., Moewes A., & Regier T. Z. Measuring partial fluorescence yield using filtered detectors. *J. Synchrotron Rad.* **21**, 716 (2014).
- 86. Achkar, A. J., Regier, T. Z., Monkman, E. J., Shen, K. M. & Hawthorn D. G. Determination of total X-ray absorption coefficient using non-resonant X-ray emission. *Sci. Rep.* **1**, 182 (2011).
- 87. Kuch, W. Imaging Magnetic Microspectroscopy. in *Magnetic Microscopy of Nanostructures*, Eds: H. Hopster H.P. Oepen, Springer-Verlag Berlin Heidelberg (2005).
- 88. Hitchcock, A. P. Soft X-ray spectromicroscopy and ptychography. *J. Electron Spectrosc. Relat. Phenom.* **200**, 49-63 (2015).
- 89. Rhensius, C. A. F. Vaz, A. Bisig, et al. Control of spin configuration in half-metallic La_{0.7}Sr_{0.3}MnO₃ nano-structures. *Appl. Phys. Lett.* **99**, 062508 (2011).
- 90. Nichols, C. I. O. et al. Microstructural and paleomagnetic insight into the cooling history of the IAB parent body. *Geochim Cosmochim Acta* **229**, 1-19 (2018).
- 91. Kuch, W., Gilles, J., Kang, S., Imada, S. & Suga, S. Magnetic-circular-dichroism microspectroscopy at the spin reorientation transition in Ni(001) films. *Phys. Rev. B* **62**, 3824 (2000).
- 92. Baldasseroni, C. et al. Temperature-driven nucleation of ferromagnetic domains in FeRh thin films. *Appl. Phys. Lett.* **100**, 262401 (2012).

- 93. Chu, Y.-H. et al. Electric-field control of local ferromagnetism using a magnetoelectric multiferroic. *Nature Materials* **7**, 478 (2008).
- 94. Ruiz-Gómez, S. et al. Direct X-ray Detection of the Spin Hall Effect in CuBi. *Phys. Rev. X* **12**, 031032 (2022).
- 95. Bryson, J. F. J. et al. Long-lived magnetism from solidification-driven convection on the pallasite parent body. *Nature* **517**, 472 (2015).
- 96. Hermann, S. et al. Imaging spin dynamics on the nanoscale using X-ray microscopy. *Frontiers in Physics* **3**, 25 (2015).
- 97. Sluka, V. et al. Emission and propagation of 1D and 2D spin waves with nanoscale wavelengths in anisotropic spin textures. *Nat Nanotechnol.* **14**, 328–333 (2019).
- 98. Foerster, M et al. Quantification of propagating and standing surface acoustic waves by stroboscopic X-ray photoemission electron microscopy. *J. Synchrotron Rad.* **26**, 184–193 (2019).
- 99. Ünal, A. A. et al. Laser-driven formation of transient local ferromagnetism in FeRh thin films. *Ultramicroscopy* **183**, 104-108 (2017).
- 100. Witte, K. et al. From 2D STXM to 3D Imaging: Soft X-ray Laminography of Thin Specimens. *Nano Lett* **20**, 1305–1314 (2020).
- 101. Bukin, N. et al. Time-resolved imaging of magnetic vortex dynamics using holography with extended reference autocorrelation by linear differential operator, *Sci. Rep.* **6**, 36307 (2016).
- 102. Martinez, M. D. P. et al. Three-dimensional tomographic imaging of the magnetization vector field using Fourier transform holography. *Phys. Rev. B* **107**, 094425 (2023).
- 103. Tromp, R. M. et al. A new aberration-corrected, energy-filtered LEEM/PEEM instrument. I. Principles and design. *Ultramicroscopy* **110**, 852-861 (2010).
- 104. Menteş, T. O. & Locatelli, A. Angle-resolved X-ray photoemission electron microscopy. *J. Electron Spectrosc. Relat. Phenom.* **185**, 323-329 (2012).
- 105. Weigand, M. et al. TimeMaxyne: A Shot-Noise Limited, Time-Resolved Pump-and-Probe Acquisition System Capable of 50 GHz Frequencies for Synchrotron-Based X-ray Microscopy. *Crystals* **12**, 1029 (2022).
- 106. Rösner, B. et al. Soft X-ray microscopy with 7 nm resolution. Optica 7, 1602 (2020).
- 107. Butcher, T. A. et al. Ptychographic Nanoscale Imaging of the Magnetoelectric Coupling in Freestanding BiFeO₃. *Advanced Materials* **36**, 2311157 (2024).
- 108. van der Laan, G. Time-resolved X-ray detected ferromagnetic resonance of spin currents. *J. Electron Spectrosc. Relat. Phenom.* **220**, 137-146 (2017).
- 109. van der Laan, G. & Hesjedal, T. X-ray detected ferromagnetic resonance techniques for the study of magnetization dynamics. *Nucl. Instrum. Meth. B* **540**, 85-93 (2023)

- 110. Cheshire, D. M. et al. Increased Gilbert damping in Yttrium Iron Garnet by low temperature vacuum annealing. arXiv:2407.16005 cond-mat.mes-hall.
- 111. Swindells, C. et al. Magnetic damping in ferromagnetic/heavy-metal systems: The role of interfaces and the relation to proximity-induced magnetism. *Phys. Rev. B* **105**, 094433 (2022).
- 112. Mendil, J. et al. Magnetic properties and domain structure of ultrathin yttrium iron garnet/Pt bilayers. *Physical Review Materials* **3**, 034403 (2019).
- 113. Cheshire, D. et al. Absence of spin-mixed states in ferrimagnet Yttrium iron garnet. *J. Appl. Phys.* **132**, 103902 (2022).
- 114. Vlachos, D., Craven, A. J. & McComb, D. W. Specimen charging in X-ray absorption spectroscopy: correction of total electron yield data from stabilized zirconia in the energy range 250–915 eV. *J. Synchrotron Rad.* **12**, 224–233 (2005).
- 115. Lebens-Higgins, Z. W. et al. Distinction between Intrinsic and X-ray-Induced Oxidized Oxygen States in Li-Rich 3d Layered Oxides and LiAlO₂, *J. Phys. Chem. C* **123**, 13201 (2019).
- 116. Yang, J. et al. Soft X-ray Induced Photoreduction of Organic Cu(II) Compounds Probed by X-ray Absorption Near-Edge (XANES) Spectroscopy. *Anal. Chem.* **83**, 7856 (2011).
- 117. Cowan, R. D. The Theory of Atomic Structure and Spectra. University of California Press, Berkeley (1981).
- 118. van der Laan, G. Hitchhiker's guide to multiplet calculations, Lect. Notes Phys. **697**, 143-200 (2006).
- 119. Caciuffo, R., Lander, G. H. & van der Laan, G. X-ray Synchrotron Radiation Techniques and their Applications to Actinide Materials. *Rev. Mod. Phys.* **95**, 015001 (2023).
- 120. Thole, B.T., van der Laan, G., & Butler, P.H. Spin-mixed ground state of Fe phthalocyanine and the temperature dependent branching ratio in X-ray absorption spectroscopy. *Chem. Phys. Lett.* **149**, 295-299 (1988).
- 121. Stavitski, E. & de Groot, F.M.F. The CTM4XAS program for EELS and XAS spectral shape analysis of transition metal L edges. *Micron* **41**, 687 (2010).
- 122.Haverkort, M. W. Quanty for core level spectroscopy excitons, resonances and band excitations in time and frequency domain. *Journal of Physics: Conference Series* **712**, 012001 (2016). Quanty, http://www.quanty.org/
- 123. de Groot, F. M. F. et al. 2p X-ray absorption spectroscopy of 3d transition metal systems. *J. Electron Spectrosc. Relat. Phenom.* **249**, 147061 (2021).
- 124. Thole, B. T., van der Laan, G. & Sawatzky, G.A. Strong magnetic dichroism predicted in the M_{4,5} X-ray absorption spectra of magnetic rare earth materials. *Phys. Rev. Lett.* **55**, 2086-2088 (1985).

- 125. van der Laan, G. & Thole, B.T. Strong magnetic X-ray dichroism in 2p absorption spectra of 3d transition metal ions. *Phys. Rev. B* **43**, 13401-13411 (1991).
- 126. Thole, B. T., Carra, P., Sette, F. & van der Laan, G. X-ray circular dichroism as a probe of orbital magnetization. *Phys. Rev. Lett.* **68**, 1943–1946 (1992). **This paper presents the sum rules linking the XMCD spectra and magnetic orbital moments.**
- 127. Carra, P., Thole, B. T., Altarelli, M. & Wang, X. X-ray Circular Dichroism and Local Magnetic Fields. *Phys. Rev. Lett.* **70**, 694-697 (1993).
- 128. Rehr, J.J. et al. Ab initio theory and calculations of X-ray spectra. *Comptes Rendus Physique* **10**, 548-559 (2009). https://feff.phys.washington.edu/
- 129. Y. Joly, Y., Ramos, A. Y., & Bunău O. Finite-difference method for the calculation of X-ray spectroscopies. In International Tables for Crystallography, Volume I, X-ray Absorption Spectroscopy and Related Techniques (2022). https://fdmnes.neel.cnrs.fr/
- 130. van der Laan, G. & Thole, B.T. Electronic correlations in Ni 2p and 3p magnetic X-ray dichroism and X-ray photoemission of ferromagnetic nickel. *J. Phys.: Condens. Matter* **4**, 4181-4188 (1992).
- 131. Dresselhauset, J. al. Antiferromagnetic coupling of Mn adsorbates to Fe(100), *Phys. Rev. B* **56**, 5461-5467 (1997)
- 132. Pearce, C. I. et al. Direct determination of cation site occupancies in natural ferrite spinels by L_{2,3} X-ray absorption spectroscopy and X-ray magnetic circular dichroism. *American Mineralogist* **91**, 880-893 (2006).
- 133. Gaudry, E. et al. From the green color of Eskolaite to the red color of Ruby: an X-ray absorption spectroscopy study. *Phys. Chem. Minerals* **32**, 710–720 (2006).
- 134. Mannini, M. et al. XAS and XMCD Investigation of Mn₁₂ Monolayers on Gold. *Chem. Eur. J.* **14**, 7530–7535 (2008).
- 135. Chen, C. T. et al. Experimental Confirmation of the X-ray Magnetic Circular Dichroism Sum Rules for Iron and Cobalt. *Phys. Rev. Lett.* **75**, 152 (1995).
- 136. Chen, C. T., Sette, F., Ma, Y. & Modesti S. Soft-X-ray magnetic circular dichroism at the L_{2,3} edges of nickel. *Phys. Rev. B* **42**, 7262(R) (1990).
- 137. Stepanow, S. et al. Giant spin and orbital moment anisotropies of a Cu-phthalocyanine monolayer. *Phys. Rev. B* **82**, 014405 (2010).
- 138. Arrio, M.-A. et al. Photoinduced Magnetization on Mo Ion in Copper Octacyanomolybdate: An X-ray Magnetic Circular Dichroism Investigation. *Journal of Physical Chemistry C* **114**, 593-600 (2010).
- 139. Agrestini, S. et al. Electronic and spin states of SrRuO₃ thin films: An X-ray magnetic circular dichroism study. *Phys. Rev. B* **91**, 075127 (2015).

- 140. Wilhelm, F. et al. Orbital and spin moments in the ferromagnetic superconductor URhGe by X-ray magnetic circular dichroism. *Phys. Rev. B* **95**, 235147 (2017).
- 141. Chaboy, J. et al. *X-ray* magnetic circular dichroism probe of the Rh magnetic moment instability in $Fe_{1-x}Rh_x$ alloys near the equiatomic concentration. *Phys. Rev. B* **59**, 3306 (1999).
- 142. Vogel, J. et al. Structure and magnetism of Pd in Pd/Fe multilayers studied by X-ray magnetic circular dichroism at the Pd L(2,3) edges. *Phys. Rev. B* **55**, 3663-3669 (1997).
- 143. Jaouen, N. et al. Electronic and magnetic interfacial states of Ag in an Ni. *J. Phys.: Condens. Matter* **20**, 095005 (2008).
- 144. Figueroa, A. I. et al. Breakdown of Hund's third rule in amorphous Co-W nanoparticles and crystalline Co₃W alloys. *Phys. Rev. B* **86**, 064428 (2012).
- 145. Sikora, M. et al. Field-induced magnetostructural phase transition in double perovskite Ca₂FeReO₆ studied via X-ray magnetic circular dichroism. *Phys. Rev. B* **79**, 220402(R) (2009).
- 146. Agrestini, S. et al. Nature of the magnetism of iridium in the double perovskite Sr₂CoIrO₆. *Phys. Rev. B* **100**, 014443 (2019).
- 147. Grange, W. et al. Experimental and theoretical X-ray magnetic-circular-dichroism study of the magnetic properties of Co₅₀Pt₅₀ thin films. *Phys. Rev. B* **62**, 1157 (2000).
- 148. Yamamoto, Y. et al. Direct Observation of Ferromagnetic Spin Polarization in Gold Nanoparticles. *Phys. Rev. Lett.* **93**, 116801 (2004) and Erratum *Phys. Rev. Lett.* **96**, 139902 (2006).
- 149. Yamamoto, Y. et al. X-ray magnetic circular dichroism study of gold nanoparticles protected by polymer. *Journal of Magnetism and Magnetic Materials* **272–276**, e1183–e1184 (2004).
- 150. Elnaggar, H. et al. Noncollinear Ordering of the Orbital Magnetic Moments in Magnetite. *Phys. Rev. Lett.* **123**, 207201 (2019).
- 151. Goedkoop, J. B. et al. Calculations of magnetic X-ray dichroism in the 3*d* absorption spectra of rare earth compounds. *Phys. Rev. B* **37**, 2086-2095 (1988).
- 152. Giorgetti C. et al. Quadrupolar Effect in X-ray Magnetic Circular Dichroism. *Phys. Rev. Lett.* **75**, 3186 (1995).
- 153. Detlefs, C. et al. Evidence for quadrupolar contributions to the circular magnetic-X-ray dichroism of rare-earths. *J. Phys. Chem. Solids* **65**, 1517 (2995).
- 154. Giorgetti, C., Dartyge, E., Baudelet, F., & Brouder C. XMCD at L_{II,III} edges of rare-earths: electric quadrupolar and dipolar effects. *Appl. Phys. A* **73**, 703–706 (2001).
- 155. Love, C. et al. Elucidation of orbital moment, anisotropy, and magnetic damping in epitaxial Fe₃O₄ films. *Phys. Rev. B* **107**, 064414 (2023).
- 156. Thakur P. et al. Direct observation of oxygen induced room temperature ferromagnetism in thin films by X-ray magnetic circular dichroism characterizations. *Appl. Phys. Lett.* **94**, 062501 (2009).

- 157. Sassi, M., Pearce, C. I., Bagus, P. S., Arenholz, E. & Rosso, K. M. First-Principles Fe L_{2,3}-Edge and O K-Edge XANES and XMCD Spectra for Iron Oxides. *J. Phys. Chem. A* **121**, 7613–7618 (2017).
- 158. Guillou, F. et al. Electronic and magnetic properties of phosphorus across the first-order ferromagnetic transition of (Mn,Fe)₂(P,Si,B) giant magnetocaloric materials. *Phys. Rev. B* **92**, 224427 (2015).
- 159. Letard, I., Sainctavit, Ph. & Deudon, C. XMCD at Fe $L_{2,3}$ edges, Fe and S K edges on Fe₇S₈. *Phys. Chem. Minerals* **34**, 113–120 (2007).
- 160. Takahashi, M. & Igarashi, J. X-ray magnetic circular dichroism at the K edge of Mn₃GaC. *Phys. Rev. B* **67**, 245104 (2003).
- 161. Duffy, L. B. et al. Magnetic proximity coupling to Cr-doped Sb₂Te₃ thin films, *Phys. Rev B* **95**, 224422 (2017).
- 162. Choi, Y. et al. Iodine orbital moment and chromium anisotropy contributions to CrI₃ magnetism. *Appl. Phys. Lett.* **117**, 022411 (2020).
- 163. Yamagami, K. et al. Itinerant ferromagnetism mediated by giant spin polarization of the metallic ligand band in the van der Waals magnet Fe₅GeTe₂. *Phys. Rev. B* **103**, L060403 (2021).
- 164. Marangolo, M. et al. Tails of near-edges X-ray absorption spectra as a fingerprint of magnetic and structural phase transitions. Application to metallic 3d ultra thin films. *J. Appl. Phys.* **93**, 5151–5155 (2003).
- 165. Liu, B. et al. Sum rule distortions in fluorescence-yield X-ray magnetic circular dichroism. *Phys. Rev. B* **96**, 054446 (2017).
- 166. Carra, P., König, H., Thole, B.T., & Altarelli, M. Magnetic X-ray dichroism: General features of dipolar and quadrupolar spectra. *Physica B* **192**, 182-190 (1993).
- 167. Goulon, J. et al. X-ray Optical Activity: Applications of Sum Rules. *Journal of Experimental and Theoretical Physics* **97**, 402–431 (2003).
- 168. Piamonteze, C., Miedema, P., & de Groot, F. M. F. Accuracy of the spin sum rule in XMCD for the transition-metal L edges from manganese to copper. *Phys. Rev. B* **80**, 184410 (2009).
- 169. Goulon, J., Goulon-Ginet, C., Cortès, R. & Dubois. J. M. On experimental attenuation factors of the amplitude of the EXAFS oscillations in absorption, reflectivity and luminescence measurements. *Journal de Physique* **43**, 539-548 (1982).
- 170. Thole, B. T. et al. 3d X-ray-absorption lines and the 3d⁹ 4fⁿ⁺¹ multiplets of the lanthanides. *Phys. Rev. B* **32**, 8 (1985).
- 171. Frazer, B. H., Gilbert, B., Sonderegger, B. R. & De Stasio G. The probing depth of total electron yield in the sub-keV range: TEY-XAS and X-PEEM. *Surface Science* **537**, 161–167 (2003).

- 172. Aksoy, F., Akgül, G., Ufuktepe, Y. & Nordlund, D. Thickness dependence of the $L_{2,3}$ branching ratio of Cr thin films. *Journal of Alloys and Compounds* **508**, 233–237 (2010).
- 173. Henneken, H., Scholze, F. & Ulm, G. Lack of proportionality of total electron yield and soft X-ray absorption coefficient. *J. Appl. Phys.* **87**, 257–268 (2000).
- 174. Hayes, TM & Boyce, JB. Extended X-ray absorption fine-structure spectroscopy. *Solid State Physics* **37**, 173-351 (1982).
- 175. Goulon, J. et al. Advanced detection systems for X-ray fluorescence excitation spectroscopy. *J. Synchrotron Rad.* **12**, 57-69 (2005).
- 176. Thole, B. T., van der Laan, G. & Fabrizio, M. Magnetic ground-state properties and spectral distributions. I. X-ray-absorption spectra. *Phys. Rev. B* **50**, 11466 (1994).
- 177. van der Laan, G., Hesjedal, T. & Bencok, P. Polarization analysis by means of individual X-ray absorption spectra of rare earths. *Phys. Rev. B* **106**, 214423 (2022).
- 178. Sainctavit, Ph., Moulin, C. C., & Arrio, M. A. Magnetic Measurements at the Atomic Scale in Molecular Magnetic and Paramagnetic Compounds. In Magnetism: Molecules to Materials I: Models and Experiments. Edited by Joel S. Miller and Marc Drillon. WILEY-VCH Verlag GmbH, p.131 (2002)...
- 179. van der Laan, G. et al. Comparison of X-ray absorption with X-ray photoemission of nickel dihalides and NiO. *Phys. Rev. B* **33**, 4253-4263 (1986).
- 180. Natoli, C. R. et al. Calculation of X-ray natural circular dichroism. Eur. Phys. J. B 4, 1–11 (1998).
- 181. Goulon, J., Goulon-Ginet, C., Cortès, R. & Dubois, J.M. On experimental attenuation factors of the amplitude of the EXAFS oscillations in absorption, reflectivity and luminescence measurements. *Journal de Physique* **43** 539-548 (1982).
- 182. Lee, J. et al. A direct test of X-ray magnetic circular dichroism sum rules for strained Ni films using polarized neutron reflection. J. Phys.: Condens. Matter 9, L137-L143 (1997).
- 183. G. van der Laan, C.M.B. Henderson, R.A.D. Pattrick, S.S. Dhesi, P.F. Schofield, E. Dudzik and D.J. Vaughan. Orbital polarization in NiFe₂O₄ measured by Ni–2p X-ray magnetic circular dichroism. *Phys. Rev. B* **59**, 4314 (1999).
- 184. Lovesey, S.W. & Collins, S.P. X-ray Scattering and Absorption by Magnetic Materials, Oxford University Press, New York, 1996.
- 185. Stöhr, J. Exploring the microscopic origin of magnetic anisotropies with X-ray magnetic circular dichroism (XMCD) spectroscopy. *J. Magn. Magn. Mater.* **200**, 470–497 (1999). **This article gives a brief review of the principles of XMCD, which are then applied to the study of the thickness-dependent electronic and magnetic properties of a Co film sandwiched between Au.**
- 186. de Groot, F. M. F. & Kotani, A. Core Level Spectroscopy of Solids. CRC Press, Boca Raton, FL (2008).

- 187. van der Laan, G. Applications of soft X-ray magnetic dichroism. *J. Phys.: Conf. Ser.* **430**, 012127 (2013).
- 188. van der Laan, G. X-ray magnetic circular dichroism, *Int. Tables Crystallogr. Vol. I,* Ch. 3.33, 508-515 (2024). https://doi.org/10.1107/S1574870722005390
- 189. van der Laan, G. Magnetic X-ray techniques, *Int. Tables Crystallogr. Vol. I, Ch.* 2.18, 169-176 (2024). https://doi.org/10.1107/S157487072200163X.
- 190. van der Laan G. & Figueroa, A.I. Magnetic ordering and its influence on X-ray spectroscopies, *Int. Tables Crystallogr. Vol. I*, Ch. 2.17, 163-168 (2024).

https://doi.org/10.1107/S1574870722001628.

- 191. Dürr, H. A., et al. Element-Specific Magnetic Anisotropy Determined by Transverse Magnetic Circular X-ray Dichroism. *Science* **277**, 213 (1997).
- 192. van der Laan, G. Microscopic origin of magnetocrystalline anisotropy in transition metal thin films. *J. Phys.: Condens. Matter* **10**, 3239-3253 (1998).
- 193. Weller, D. et al. Microscopic origin of magnetic anisotropy in Au/Co/Au probed with X-ray magnetic circular dichroism. *Phys. Rev. Lett.* **75**, 3752 (1995).
- 194. Bruno, P. Tight-binding approach to the orbital magnetic moment and magnetocrystalline anisotropy of transition-metal monolayers. *Phys. Rev. B* **39**, 865 (1989).
- 195. Pizzini, S. et al. Evidence for the Spin Polarization of Copper in Co /Cu and Fe /Cu Multilayers. *Phys. Rev. Lett.* **74**, 1470 (1995).
- 196. Held, G. A. et al. *X-ray* magnetic circular dichroism study of the induced spin polarization of Cu in Co/Cu and Fe/Cu multilayers. *Zeitschrift für Physik B* **100**, 335 (1996).
- 197. Kuch, W. et al. Artificially ordered FeCu alloy superlattices on Cu(001). II. Spin-resolved electronic properties and magnetic dichroism. *Phys. Rev. B* **58**, 8556 (1998).
- 198. Offi, F. et al. Induced Fe and Mn magnetic moments in Co-FeMn bilayers on Cu(001). *Phys. Rev. B* **67**, 094419 (2003).
- 199. Abrudan, R. et al. Structural and magnetic properties of epitaxial Fe/Co $_x$ O bilayers on Ag(001). *Phys. Rev. B* **77**, 014411 (2008).
- 200. Ebert H. & Man'kovsky S., Field-Induced Magnetic Circular X-ray Dichroism in Paramagnetic Solids: A New Magneto-Optical Effect. *Phys. Rev. Lett.* **90**, 077404 (2003).
- 201. Gambardella, P. et al. Ferromagnetism in one-dimensional monatomic metal chains. *Nature* **416**, 301 (2002).
- 202. Gambardella, P. et al. Localized Magnetic States of Fe, Co, and Ni Impurities on Alkali Metal Films. *Phys. Rev. Lett.* **88**, 047202 (2002).

- 203. Donati, F. et al. Magnetic remanence in single atoms. *Science* **352**, 318–321 (2016). **An XMCD** study toward single atomic memory.
- 204. Vaz, C. A. F. et al. Multiplicity of magnetic domain states in circular elements probed by photoemission electron microscopy. *Phys. Rev. B* **72**, 224426 (2005).
- 205. Kronast, F. et al. Element-specific magnetic hysteresis of individual 18 nm Fe nanocubes. *Nano Lett.* **11**, 1710–1715 (2011).
- 206. Balan, A. et al. Direct Observation of Magnetic Metastability in Individual Iron Nanoparticles. *Phys. Rev. Lett.* **112**, 107201 (2014).
- 207. Kleibert, A. et al. Direct observation of enhanced magnetism in individual size- and shape-selected 3d transition metal nanoparticles. *Phys. Rev. B* **95**, 195404 (2017).
- 208. Vijayakumar, J. et al. Absence of a pressure gap and atomistic mechanism of the oxidation of pure Co nanoparticles. *Nature Communications* **14**, 174 (2023).
- 209. Boulle, O. et al. Room-temperature chiral magnetic skyrmions in ultrathin magnetic nanostructures. *Nature Nanotechnology* **11**, 449 (2016).
- 210. Woo, S. et al. Spin-orbit torque-driven skyrmion dynamics revealed by time-resolved X-ray microscopy. *Nature Communications* 8, 15573 (2017).
- 211. Hierro-Rodriguez, A. et al. Revealing 3D magnetization of thin films with soft X-ray tomography: magnetic singularities and topological charges. *Nature Comms*. **11**, 6382 (2020).
- 212. van der Laan, G. Determination of spin chirality using X-ray magnetic circular dichroism. *Phys. Rev. B* **104**, 094414 (2021).
- 213. Herguedas-Alonso, A. E. et al. A fast magnetic vector characterization method for quasi two-dimensional systems and heterostructures. *Scientific Reports* **13**, 9639 (2023).
- 214. Šmejkal, L., Sinova, J. & Jungwirth, T. Emerging research landscape of altermagnetism. *Phys. Rev. X* **12**, 040501 (2022).
- 215. Hariki et al. X-ray magnetic circular dichroism in altermagnetic α -MnTe. Phys. Rev. Lett. **132**, 176701 (2024).
- 216. Amin, O. J. et al. Nanoscale imaging and control of altermagnetism in MnTe. *Nature* **636**, 348 (2024).
- 217. Abdeldaim, A. H. et al. Kitaev interactions through extended superexchange pathways in the j_{eff} = 1/2 Ru³⁺ honeycomb magnet RuP₃SiO₁₁. *Nature Communications* **15**, 9778 (2024).
- 218. Qi, X.-L. & Qi, S.-C. Topological insulators and superconductors. *Rev. Mod. Phys.* **83**, 1057 (2011).
- 219. Nadj-Perge, S. et al. Observation of Majorana fermions in ferromagnetic atomic chains on a superconductor. *Science* **346**, 602 (2014).

- 220. Qin Liu, Q., Liu, C. X, Xu, C, Qi, X.-L., & Zhang, S.-C. Magnetic Impurities on the Surface of a Topological Insulator. *Phys. Rev. Lett.* **102**, 156603 (2009).
- 221. Figueroa, A. I. et al. X-ray magnetic circular dichroism study of Dy-doped Bi₂Te₃ topological insulator thin films. *J. Magn. Magn. Mater.* **422**, 93-99 (2017).
- 222. Katmis, F. et al. A high-temperature ferromagnetic topological insulating phase by proximity coupling. *Nature* **533**, 513 (2016).
- 223. Liu, V. Y. et al. Coherent Epitaxial Semiconductor–Ferromagnetic Insulator InAs/EuS Interfaces: Band Alignment and Magnetic Structure. *ACS Appl. Mater. Interfaces* **12**, 8780 (2019).
- 224. Scheybal, A. et al. Induced magnetic ordering in a molecular monolayer. *Chem. Phys. Lett.* **411**, 214–220 (2005).
- 225. Sanvito, S. The rise of spinterface science. Nat. Phys. 6, 562–564 (2010).
- 226. Cinchetti, M., Dediu, V. A. & Hueso, L. E. Activating the molecular spinterface. *Nature Mater.* **16**, 507–515 (2017).
- 227. Bernien, M. et al. Tailoring the Nature of Magnetic Coupling of Fe-Porphyrin Molecules to Ferromagnetic Substrates, *Phys. Rev. Lett.* **102**, 047202 (2009).
- 228. Hermanns, C. F. et al, Magnetic Coupling of Porphyrin Molecules Through Graphene, *Adv. Mater.* **25**, 3473 (2013).
- 229. Wäckerlin, C. et al. Giant Hysteresis of Single-Molecule Magnets Adsorbed on a Nonmagnetic Insulator. *Adv. Mater.* **28**, 5195 (2016).
- 230. Marocchi, S. et al. Relay-Like Exchange Mechanism through a Spin Radical between TbPc₂ Molecules and Graphene/Ni(111) Substrates, *ACS Nano* **10**, 9353–9360 (2016).
- 231. Candini, A., Klar, D., Marocchi, S. et al. Spin-communication channels between Ln(III) bisphthalocyanines molecular nanomagnets and a magnetic substrate, *Sci. Rep.* **6**, 21740 (2016).
- 232. Huttmann, F. et al. Europium Cyclooctatetraene Nanowire Carpets: A Low-Dimensional, Organometallic, and Ferromagnetic Insulator. *Phys. Chem. Lett.* **10**, 911–917 (2019).
- 233. Kumar, K.S. & Ruben, M., Sublimable Spin-Crossover Complexes: From Spin-State Switching to Molecular Devices. *Angew. Chem. Int. Ed.* **60**, 7502–7521 (2021).
- 234. Grunwald, J. et al. Defying the inverse energy gap law: a vacuum-evaporable Fe(II) low-spin complex with a long-lived LIESST state. Chem. Sci. **14**, 7361-7380 (2023).
- 235. Hellman, F. et al. Interface-Induced Phenomena in magnetism, *Rev. Mod. Phys.* **89**, 025006 (2017).
- 236. Bonetti, S. et al. Direct observation and imaging of a spin-wave soliton with p-like symmetry, *Nature Communications* **6**, 8889 (2015).

- 237. Kirilyuk, A., Kimel, A. V., & Rasing, T. Ultrafast optical manipulation of magnetic order, *Rev. Mod. Phys.* **82**, 2731 (2010).
- 238. Stamm, C. et al. W. Eberhardt, Femtosecond modification of electron localization and exchange of angular momentum in Ni, *Nature Materials* **6**, 740 (2007).
- 239. Boeglin, C. et al. Distinguishing the ultrafast dynamics of spin and orbital moments in solids, *Nature* **465**, 458 (2010).
- 240. Dornes, C. et al. The ultrafast Einstein-de Haas effect. Nature 565, 209-212 (2019).
- 241. Radu, I. et al. Transient ferromagnetic-like state mediating ultrafast reversal of antiferromagnetically coupled spins. *Nature* **472**, 205 (2011).
- 242. Pontius, N., Holldack, K., Schüßler-Langeheine, C., Kachel, T. & Mitzner, R. The FemtoSpeX facility at BESSY II, *Journal of large-scale research facilities (JLSRF)* **2**, A46 (2016).
- 243. Higley, D. J. et al. Femtosecond X-ray magnetic circular dichroism absorption spectroscopy at an X-ray free electron laser, *Rev. Sci. Instrum.* **87**, 033110 (2016).
- 244. Lutman, A. A. et al. Polarization Control in an X-ray Free-Electron Laser, *Nature Photonics* **10**, 468 (2016).
- 245. Wang, T. et al. Femtosecond Single-shot X-ray Imaging of Nanoscale Ferromagnetic Order, *Phys. Rev. Lett.* **108**, 267403 (2012).
- 246. Graves, C. E. et al. Nanoscale spin reversal by nonlocal angular momentum transfer following ultrafast laser excitation in ferrimagnetic GdFeCo, *Nature Materials* **12**, 293 (2013).
- 247. Le Guyader, L. et al. State-resolved ultrafast charge and spin dynamics in Co/Pd multilayers, *Appl. Phys. Lett.* **120**, 032401 (2022).
- 248. Willems, F. et al. Optical inter-site spin transfer probed by energy and spin-resolved transient absorption spectroscopy, *Nature Commun.* **11**, 871 (2020).
- 249. van der Laan, G. Sum rule practise, J. Synchrotron Rad. **6**, 694-695 (1999).
- 250. Altarelli, M., & Sainctavit, Ph. Sum rules for XMCD, in *Magnetism and Synchrotron Radiation*, page 65-74, Ed. de Physique (1997).
- 251. Nesvizhskii, A. I., Ankudinov, A. L., & Rehr, J. J. Normalization and convergence of X-ray absorption sum rules. *Phys. Rev. B* **63**, 094412 (2001).
- 252. Altarelli, M., Sum rules for X-ray magnetic circular dichroism. *Il Nuovo Cimento* **20D**, 1067 (1998).
- 253. Kowalik, I. A. Element Specific Magnetometry Combining X-ray Circular with Linear Dichroism: Fundamentals and Applications. *Acta Physica Polonica A* **127**, 831 (2015).
- 254. Wende, H. Recent advances in X-ray absorption spectroscopy. *Rep. Prog. Phys.* **67**, 2105 (2004). An advanced-level review of XAS and its applications to a wide class of materials systems.

- 255. Funk, T., Deb, A., George, S. J., Wang H. X. & Cramer S. P., X-ray magnetic circular dichroism—a high energy probe of magnetic properties. *Coord. Chem. Rev.* **249**, 3 (2005).
- 256. de Groot, F. M. F. J. X-ray absorption and dichroism of transition metals and their compounds. *J. Electron Spectrosc. Relat. Phenom.* **67**, 529 (1994).
- 257. Wu, R. Q., Wang, X. D. & Freeman, A. J. First principles investigation of the validity and range of applicability of the X-ray magnetic circular dichroism sum rule. *Phys. Rev. Lett.* **71**, 3581 (1993).
- 258. van Veenendaal, M., Goedkoop, J. B., & Thole, B. T. Branching Ratios of the Circular Dichroism at Rare Earth L₂₃ Edges. *Phys. Rev. Lett.* 78, 1162 (1997).
- 259. Figueroa, A.I. et al., Magnetic Cr doping of Bi₂Se₃: Evidence for divalent Cr from X-ray spectroscopy. *Phys. Rev B* **90**, 134402 (2014).
- 260. Wu, R. Q. & Freeman, A. J. Limitation of the Magnetic-Circular-Dichroism Spin Sum Rule for Transition Metals and Importance of the Magnetic Dipole Term. *Phys. Rev. Lett.* **73**, 1994 (1994).
- 261. Miura, Y. and Okabayashi, J. Understanding magnetocrystalline anisotropy based on orbital and quadrupole moments. *J. Phys.: Condens. Matter* **34**, 473001 (2022).
- 262. Stohr, J. & Konig H. Determination of spin-moment and orbital-moment anisotropies in transition-metals by angle-dependent X-ray magnetic circular-dichroism. *Phys. Rev. Lett.* **75**, 3748-3751 (1995).
- 263. Arvanitis, D. et al. Experimental determination of orbital and spin moments from MCXD on 3d metal overlayers. in *Spin-orbit influenced spectroscopies of magnetic solids*, Eds: Ebert, H. & Schutz, G. Springer Verlag, Berlin (1996).
- 264. Sainctavit, Ph., Arrio, M. A. & Brouder, C. Analytic calculation of the spin sum-rule at the $L_{2,3}$ edges of Cu^{2+} . *Phys. Rev. B* **52**, 12766-12769 (1995).
- 265. Sainctavit, Ph. Magnetic operators for Ti³⁺ and Cu²⁺ ground states. *J. Electron Spectrosc. Relat. Phenom.* **86**, 133-138 (1997).
- 266. Edmonds, K.W. et al. Ferromagnetic moment and antiferromagnetic coupling in (Ga,Mn)As thin films, *Phys. Rev. B* **71**, 064418 (2005).
- 267. van der Laan, G. & Thole, B.T. X-ray-absorption sum rules in jj-coupled operators and ground-state moments of actinide ions. *Phys. Rev. B* **53**, 14458-14469 (1996).
- 268. van der Laan, G. and Thole, B. T. Angular dependent photoelectric yield. Measurement of the La 3d Auger and autoionization lifetime widths. *J. Electron Spectrosc. Relat. Phenomen.* **46**, 123 129 (1988).
- 269. Fauth K. How well does total electron yield measure X-ray absorption in nanoparticles? *Appl. Phys. Lett.* **85**, 3271–3273 (2004).

- 270. Noma, A. I. Correction of the Self-Absorption Effect in Fluorescence X-ray Absorption Fine Structure. *Jpn. J. Appl. Phys.* **32**, 2899–2902 (1993).
- 271. Tröger, L. et al. Full correction of the self-absorption in soft-fluorescence extended X-ray-absorption fine structure. *Phys. Rev. B* **46**, 3283–3289 (1992).
- 272. Vaz, C. A. F., Moutafis, C., Quitmann, C. & Raabe J. Luminescence-based magnetic imaging with scanning X-ray transmission microscopy. *Appl. Phys. Lett.* **101**, 083114 (2012).
- 273. Vaz, C. A. F., Moutafis, C., Buzzi, M. & Raabe J. X-ray excited optical luminescence of metal oxide single crystals. *J. Electron Spectrosc. Relat. Phenom.* **189**, 1-4 (2013).
- 274. Kallmayer, M. et al. Interface magnetization of ultrathin epitaxial $Co_2FeSi(110)/Al_2O_3$ films. *J. Phys. D: Appl. Phys.* **40**, 1552–1557 (2007).
- 275. Stenning, G. B. G. et al. Transverse magnetic exchange springs in a DyFe₂/YFe₂ superlattice. *Phys. Rev. B* **86**, 174420 (2012).
- 276. Fert, A. Reyren, N. & Cros, V. Magnetic skyrmions: advances in physics and potential applications. *Nature Reviews Materials* **2**, 17031 (2017).
- 277. Tokura, Y. & Kanazawa, N. Magnetic Skyrmion Materials. *Chem. Rev.* **121**, 2857–2897 (2021).
- 278. Ajayi, T. M. et al. Characterization of just one atom using synchrotron X-rays. Nature **618**, 69 (2023).
- 279. Zhu, X. et al. Measuring spectroscopy and magnetism of extracted and intracellular magnetosomes using soft X-ray ptychography. PNAS **113**, E8219 (2016).
- 280. Moyer, J. A. et al. Magnetic structure of Fe-doped CoFe₂O₄ probed by X-ray magnetic spectroscopies. *Phys. Rev. B* **84**, 054447 (2011).

Acknowledgements

A.F.R. acknowledges financial support from the Spanish MICIIN (PID2021-127397NB-I00), Catalan AGAUR (2021SGR00328) and EU FEDER funds.

Author contributions

Introduction (C.A.F.V., G.v.d.L., G.S.); Experimentation (G.v.d.L., S.C., F.K., E.W., F.W.); Results (G.v.d.L., Ph.S.); Applications (C.A.F.V., H.A.D., W.K., H.W.); Reproducibility and data deposition (C.A.F.V.); Limitations and optimizations (C.A.F.V., G.v.d.L., A.F.R., Ph.S.); Outlook (C.A.F.V., G.v.d.L., A.F.R., G.S.); overview of the Primer (all authors).

Competing interests

The authors declare no conflicts of interest.

Peer review information

Nature Reviews Methods Primers thanks Daniel Haskel, Javier Herrero-Martin and the other, anonymous, reviewer(s) for their contribution to the peer review of this work.

Related links

Database of X-ray interactions with matter: https://henke.lbl.gov/optical_constants/

Quanty, code to calculate XMCD: http://www.quanty.org/

FEFF, code to calculate XAS: https://feff.phys.washington.edu/

FDMNES, code to calculate XAS: https://fdmnes.neel.cnrs.fr/

Supplementary information

[file supplied]

Glossary

Absorption edge

Sudden increase in X-ray absorption at photon energies corresponding to electron transitions from core level to empty states.

Circularly polarized photon

A particle of light whose electric field rotates in a circular pattern, as the particle moves forward.

E1 electric-dipole transitions

Quantum processes in which an electron moves between energy levels in an atom or molecule by absorbing or emitting a photon, resulting in a change in the dipole moment.

E2 electric-quadrupole transitions

Quantum processes involving the movement of an electron between energy levels in an atom or molecule that cause a change in the electric quadrupole moment. These transitions typically have lower probability than E1 transitions.

Hard X-rays

High-energy X-ray radiation with short wavelengths. Hard X-rays can penetrate dense materials, making them useful for imaging and analysis in various fields, including medical and industrial applications.

Magnetic soliton

Stable, wave-like structure in a magnetized material; the magnetic spins twist in a specific pattern and move without changing shape over time.

Magneto-optical effects

Magneto-optical effects describe the changes in a material's optical properties — such as how it absorbs or reflects light — in the presence of a magnetic field.

Soft X-rays

A type of X-ray radiation with lower energy and longer wavelengths, compared with regular or hard X-rays, making them useful for studying materials at shallow depths or with delicate structures.

Spin-polarized electron

An electron whose spin — a quantum property similar to magnetic orientation — is aligned in a specific direction, either up or down, rather than in a random direction.

Tender X-rays

A type of X-ray radiation with energy between soft and hard X-rays, which hence penetrate deeper than soft X-rays.

X-ray helicity

The direction of the rotation (left, corresponding to negative helicity or right, corresponding to positive helicity) of the electric field in circularly polarized X-rays.

X-ray magnetic cross-section

Quantifies the probability of X-rays interacting with a material's magnetic electrons, providing insights into its magnetic properties.

	XPEEM	TXM	STXM	XRH	XRPty
Resolution	25–50 nm	25–50 nm	10–30 nm	20 nm	5 nm
Depth	1–10nm	Bulk	Bulk	Bulk	Bulk
Sample	Conductive,	Thin	Thin	Thin	Thin
requirements	flat				
Tomography	Limited	✓	✓	✓	✓
Magnetic field	<10 mT	✓	✓	✓	✓

Table 1. Main characteristics of microscopy techniques (XPEEM: X-ray photoemission electron microscopy, TXM: transmission X-ray microscopy, STXM: scanning transmission X-ray microscopy, XRH: X-ray holography, XRPty: X-ray ptychography).

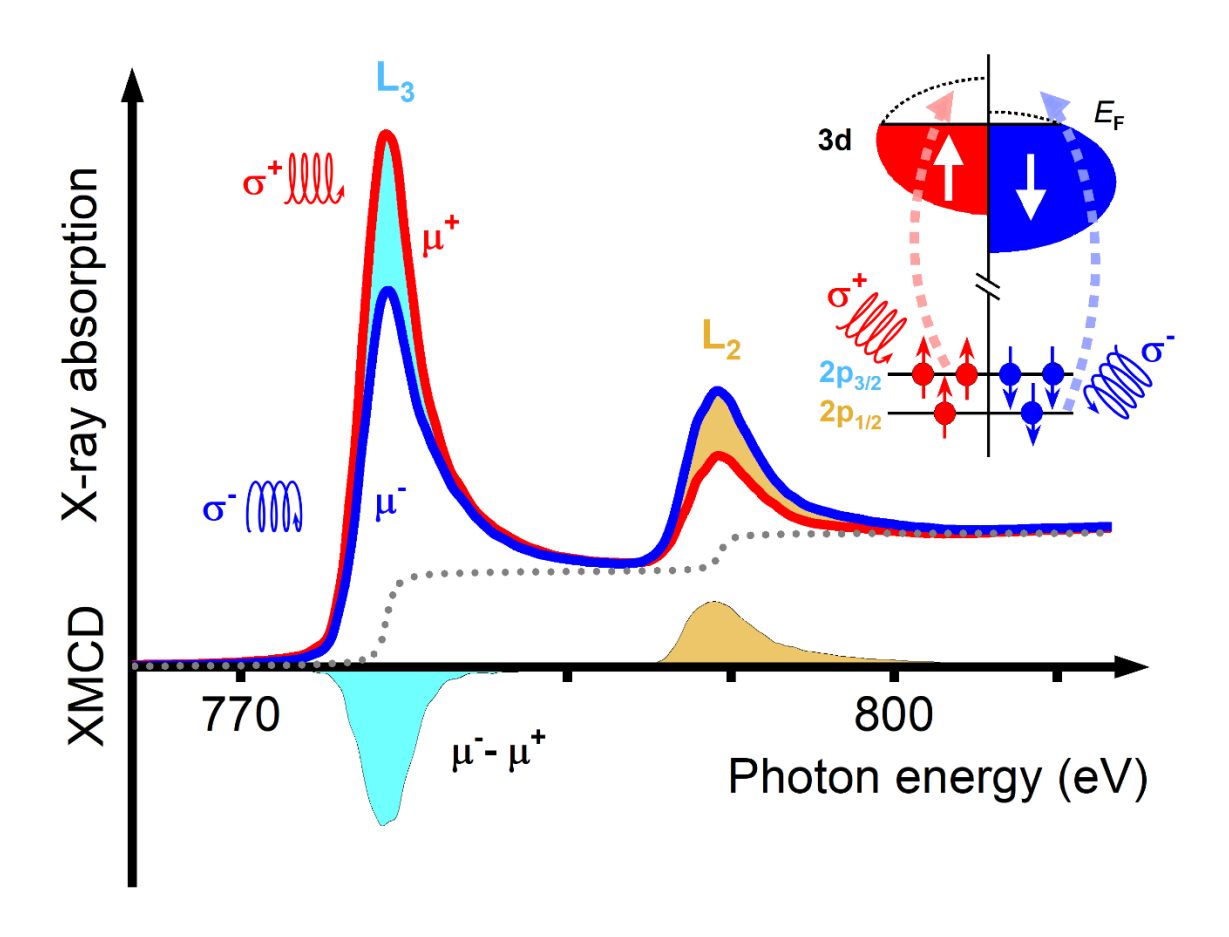


Fig. 1: X-ray magnetic circular dichroism (XMCD). For a magnetic metal (Co), the spectrum of X-ray absorption shows two peaks known as the L_2 and L_3 edges corresponding to atomic transitions from core $2p_{1/2}$ and $2p_{3/2}$ to empty 3d states. Absorption is different for left-circularly polarized X-rays (negative helicity σ^- , blue line) compared with right-circularly polarized X-rays (positive helicity σ^+ , red line): as illustrated in the inset, spin-up electrons from the $2p_{3/2}$ level are preferably excited with X-rays of positive helicity (σ^+) instead of negative helicity (σ^-); spin-down electrons from the $2p_{1/2}$ level are preferably excited with X-rays of negative helicity (σ^-); when there is also an imbalance of empty spin states in the valence band (above E_F , the Fermi energy), absorption is different for each of the X-ray polarizations. This is XMCD, and, as indicated on the horizontal axis, the sign of the difference changes between the L_3 and L_2 edges if the spin moment is larger than the orbital moment. The dotted line shows the contribution arising from transitions to the continuum.

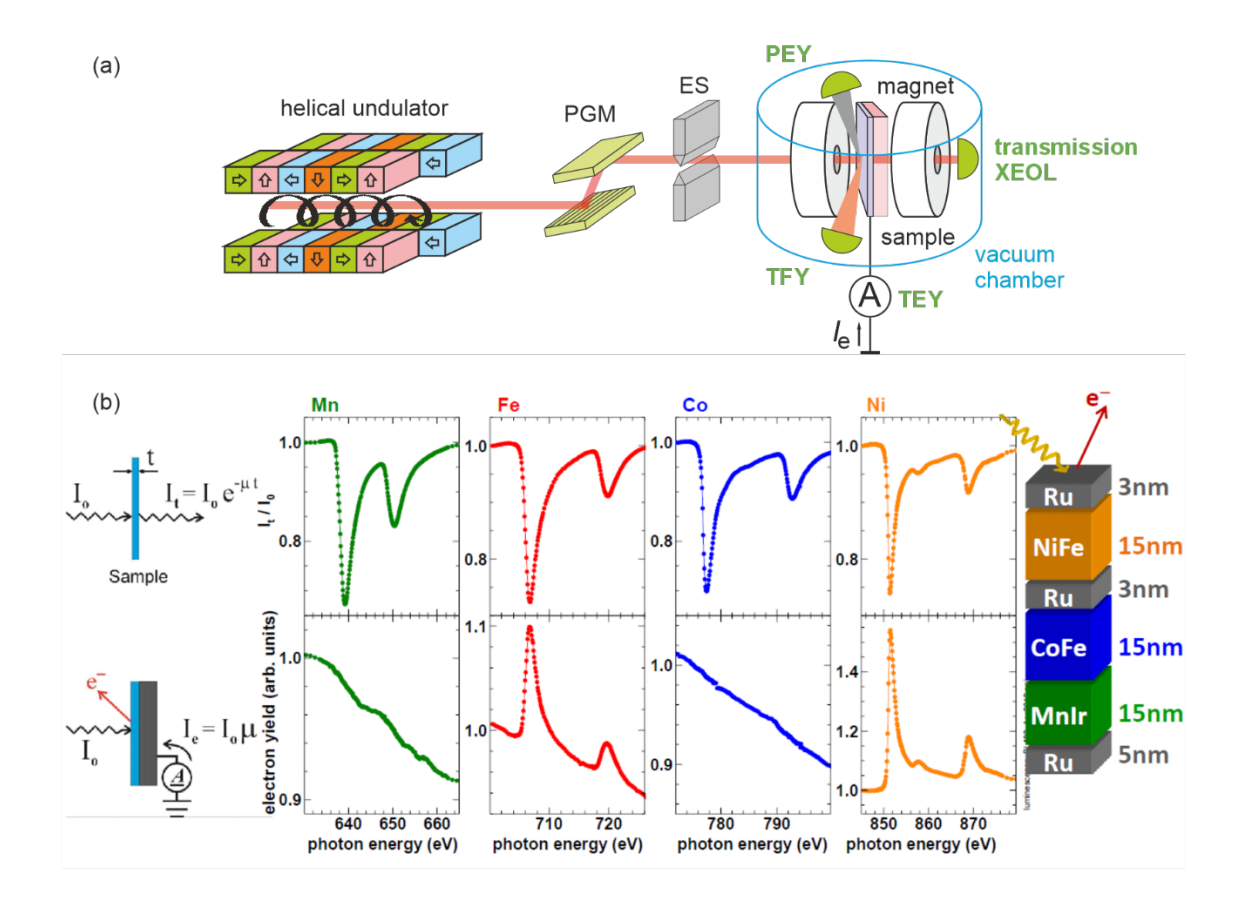


Fig. 2: Experimental set-up and variety of detection modes. a, The instrumental setup, showing the basic key components — helical undulator, planar grating monochromator and exit slit — and the sample environment that enables various detection modes: transmission, total electron yield (TEY), total fluorescence yield (TFY), partial electron yield (PEY), and X-ray-excited optical luminescence (XEOL). **b,** Spectra for transmission (top panels) and TEY (bottom panels) are compared at the $L_{2,3}$ edges of Mn, Fe, Co and Ni in the multilayer structure indicated on the right. Transmission intensity I_t for material thickness t, and the TEY I_e are related to the incident intensity I_0 through the X-ray absorption coefficient μ (left). The absence of a TEY signal at the Mn and Co edges reflects the short escape depth of electrons from the sample despite the longer penetration length of the X-rays. Part **b**, image courtesy of Elke Arenholz.

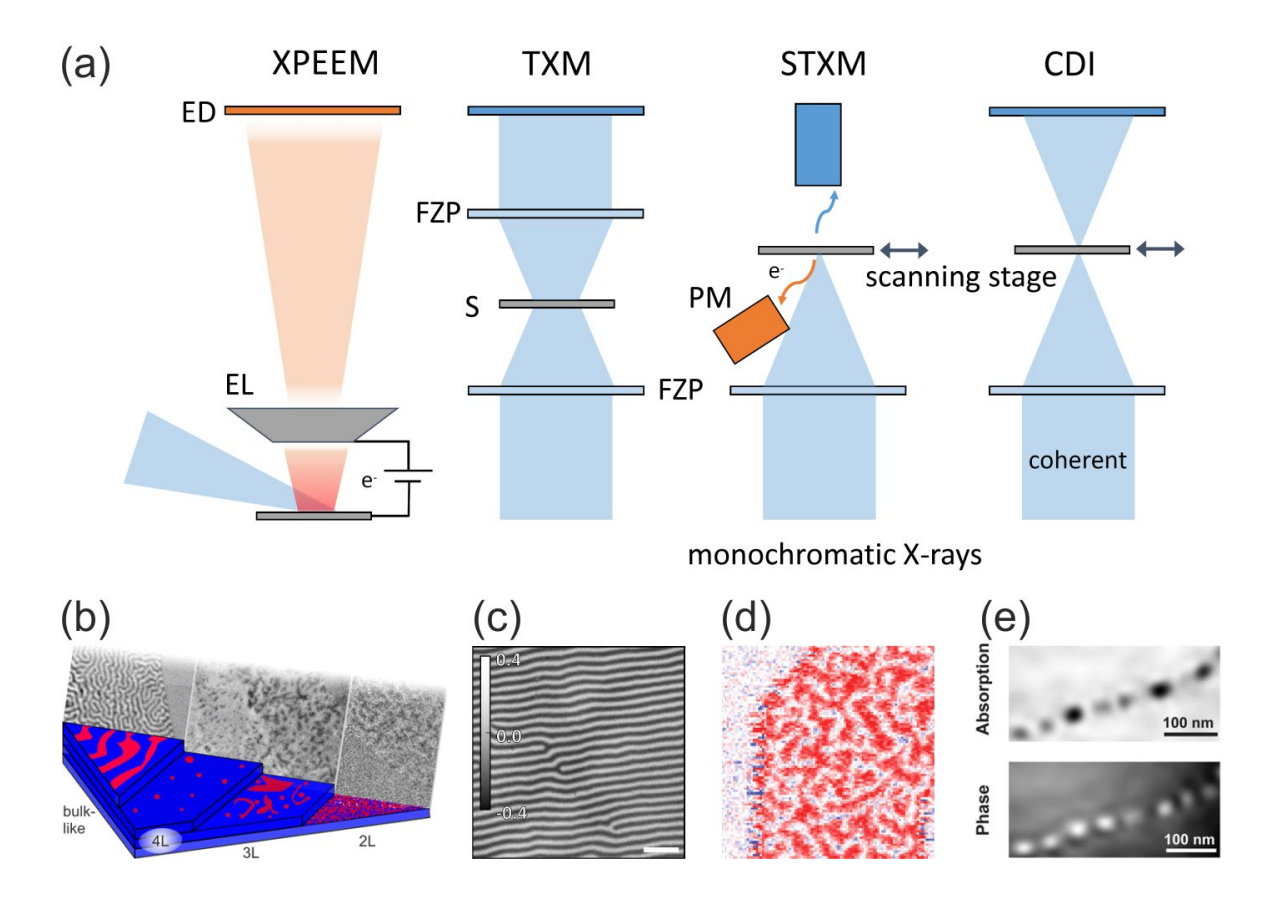


Fig. 3: Imaging and dynamical techniques related to X-ray magnetic circular dichroism (XMCD). a,

Schematics of four XMCD-related techniques: X-ray photoemission electron microscopy (XPEEM), transmission X-ray microscopy (TXM), scanning transmission X-ray microscopy (STXM), and coherent diffraction imaging (CDI). Blue represents the path of the X-rays, red hue that of imaging electrons in XPEEM. FZP, Fresnel zone plate; PM, photomultiplier. **b**, XPEEM images of the XMCD contrast (greyscale) at the Fe L₃ edge show the magnetic domain structure of Fe₅GeTe₂ films as a function of layer thickness (shown schematically in the colour image) 23 . **c**, TXM magnetic image of a Ni₈₀Fe₂₀/NdCo₅/Ni₈₀Fe₂₀ trilayer structure, each layer 80 nm thick, grown on a 50-nm Si₃N₄ membrane (scale bar 1 μ m) 211 . **d**, STXM magnetic image showing skyrmion textures in Ir–Co–Pt asymmetric multilayers 11 (image size is $1.5 \times 1.5 \ \mu$ m²). **e**, Reconstructed XMCD signals — absorption (top) and phase (bottom) — from ptychography (a form of CDI) from a single magnetosome chain of a magnetotactic bacteria 279 . Part **b** adapted from ref. 23 , CC BY 4.0

(https://creativecommons.org/licenses/by/4.0/). Part c reprinted from ref. ²¹¹, Springer Nature Limited. Part d reprinted from ref. ¹¹, Springer Nature Limited. Part e adapted with permission from ref. ²⁷⁹, National Academy of Sciences.

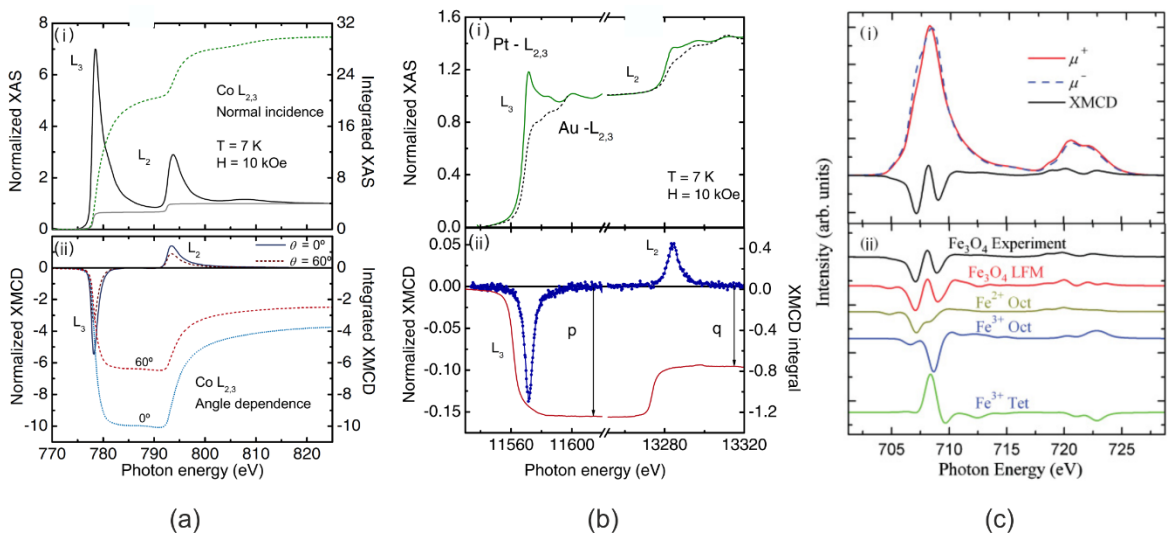


Fig. 4: Examples of spectra from X-ray absorption spectroscopy (XAS) and X-ray magnetic dichroism (XMCD). a, The XAS spectrum of a magnetite film, Fe₃O₄/MgO(001) is different for right and left circularly polarized X-rays; the corresponding XMCD spectrum is indicated by the solid black line, showing a complex structure due to the contributions from different cation species. These can be decomposed by using ligand field multiplet (LFM) theory, highlighting the antiferromagnetic coupling between spins on the octahedral and tetrahedral Fe sites, manifest in the opposite sign of the XMCD ²⁸⁰. XAS and XMCD spectra are shown for perpendicularly magnetized Co/Pt multilayers at the Co (b) and Pt (c) L_{2,3} edges, demonstrating induced magnetism in paramagnetic Pt due to proximity effects ²⁹. **b,** In the upper panel, the isotropic XAS signal (solid line) of Co is shown for normally incident X-rays (T, temperature; H, applied field). The XAS background signal (grey line) is removed before calculating the integrated XAS signal; the integrated signal (dashed line) goes into the spin and orbital moment determination, performed using the XMCD sum rules. The lower panel shows the dependence of the XMCD signal with the angle of incidence of the X-rays (solid line for normal incidence, dashed line for 60° from the normal) used to estimate the in-plane and out of plane orbital moment components, $m_L(\theta) = m_L^{\parallel} \sin^2 \theta + m_L^{\perp} \cos^2 \theta$. The bottom dotted and dashed lines show the respective integrated signal. The integrated signal (proportional to $m_{\rm L}$) demonstrates a larger orbital moment along the out of plane direction. c, For Pt, the normalized XAS spectra have less pronounced peaks than for Co (3d⁷4s²) due to the lower density of empty states of Pt, with a configuration 5d⁹6s¹; the spectrum of Au, with a full 5d band is shown to further illustrate this point. The XMCD signal (data points, lower panel) is shown with the integrated signal (red line) used for the moment calculation with the XMCD sum rules; p and q are the integrated areas under the L₃ peak and the total XMCD area, respectively, used to calculate the spin and orbital moments Part a adapted with permission from ref. ²⁸⁰, American Physical Society. Parts **b**, **c** adapted with permission from ref. ²⁹, American Physical Society.

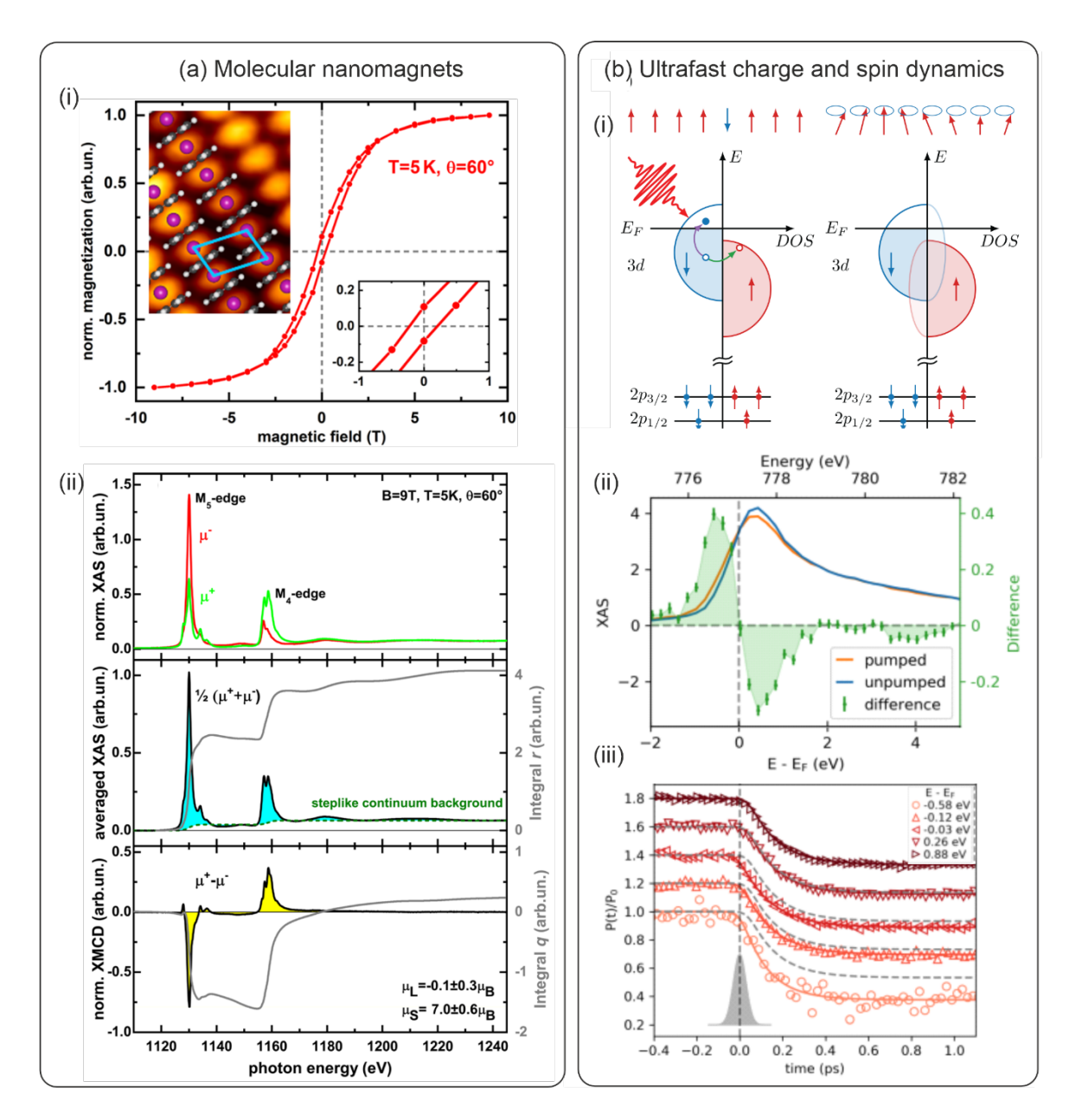


Fig. 5: X-ray magnetic circular dichroism (XMCD) for the study of magnetic molecular systems, and ultrafast charge and spin dynamics. a, The field-dependence of the XMCD signal at the Eu M_5 edge of europium cyclooctatetraene nanowires on graphene demonstrating an open loop of the magnetic hysteresis, i.e., a remanent magnetization at zero applied magnetic field; the inset shows the topography obtained from scanning tunnelling microscopy. b, Polarization-resolved X-ray absorption spectra (XAS, top), average XAS (middle) and XMCD (bottom) at the Eu $M_{4,5}$ edges (μ^+ , μ^- : right, left circular polarization) and integrated XAS and XMCD signal used for calculating the spin (7.0±0.6 μ_B/Gd) and orbital (0.1±0.3 μ_B/Gd) moments from the sum rules (grey lines) ²³². B, applied magnetic field; T, temperature; ϑ , angle of X-ray incidence. c, Schematic of the state-resolved charge and spin dynamics process: after the creation of a hole in the majority band by an ultrafast optical light excitation (pumping, violet arrow), a spin-flipping scattering event moves the hole from the majority

to the minority band (green arrow); the flipped spin thermalizes afterwards into spin waves. Since XAS probes empty density of states (DOS, schematically shown here as a function of energy, E), it can be used to probe the light-induced hole states. **d**, XAS spectra for unpumped and pumped states in Co/Pd multilayers, and the difference between them: the change in sign of this difference corresponds to the value of E_F . **e**, Around E_F , ultrafast spin depolarization can be detected at different positions within the electron bands by tracking the evolution of the magnetic polarization P (proportional to the XMCD signal) at time t, P_0 is the polarisation in the unpumped state) 247 . Parts **a**, **b** adapted with permission from ref. 232 , © 2019 American Chemical Society. Parts **c**, **d**, **e** adapted from ref. 247 , CC BY 4.0 (https://creativecommons.org/licenses/by/4.0/).